Elongasome core proteins and class A PBP1a display zonal, processive movement at the midcell of *Streptococcus pneumoniae*

Amilcar J. Perez[a1], Melissa M. Lamanna[a1], Kevin E. Bruce[a1], Marc A. Touraev[a], Julia E. Page[b], Sidney L. Shaw[a], Ho-Ching Tiffany Tsui[a], and Malcolm E. Winkler[a2]

[a]Department of Biology, Indiana University Bloomington, Bloomington, IN 47405; [b]Department of Microbiology, Blavatnik Institute, Harvard Medical School, Boston, MA 02115

[1]A.J.P., M.M.L. and K.E.B. contributed equally to this work.

Running title: Dynamics of pneumococcal peripheral PG synthesis

Key words: processive movement of PG synthesis proteins; PBP2b:RodA:MreC elongasome dynamics; Class A PBP circumferential movement; MpgA muramidase confined subdiffusion; diffusion of non-active PG synthesis proteins

[2]Corresponding author:

Malcolm E. Winkler
Department of Biology
Indiana University Bloomington
1001 East Third Street
Bloomington, Indiana 47405 USA
Phone: 812-856-1318
Email: winklerm@indiana.edu

ABSTRACT

Ovoid-shaped bacteria, such as *Streptococcus pneumoniae* (pneumococcus), have two spatially separated peptidoglycan (PG) synthase nanomachines that locate zonally to the midcell of dividing cells. The septal PG synthase bPBP2x:FtsW closes the septum of dividing pneumococcal cells, whereas the elongasome located on the outer edge of the septal annulus synthesizes peripheral PG outward. We showed previously by sm-TIRFm that the septal PG synthase moves circumferentially at midcell, driven by PG synthesis and not by FtsZ treadmilling. The pneumococcal elongasome consists of the PG synthase bPBP2b:RodA, regulators MreC, MreD, and RodZ, but not MreB, and genetically associated proteins Class A aPBP1a and muramidase MpgA. Given its zonal location separate from FtsZ, it was of considerable interest to determine the dynamics of proteins in the pneumococcal elongasome. We found that bPBP2b, RodA, and MreC move circumferentially with the same velocities and durations at midcell, driven by PG synthesis. However, outside of the midcell zone, the majority of these elongasome proteins move diffusively over the entire surface of cells. Depletion of MreC resulted in loss of circumferential movement of bPBP2b, and bPBP2b and RodA require each other for localization and circumferential movement. Notably, a fraction of aPBP1a molecules also moved circumferentially at midcell with velocities similar to those of components of the core elongasome, but for shorter durations. Other aPBP1a molecules were static at midcell or diffusing over cell bodies. Last, MpgA displayed non-processive, subdiffusive motion that was largely confined to the midcell region and less frequently detected over the cell body.

SIGNIFICANCE

These results demonstrate that unlike in rod-shaped bacteria, the core elongasome of *S. pneumoniae* exhibits zonal, circumferential motion. This motion is independent of FtsZ treadmilling or the presence of MreB filaments and is separate from the circumferential motion of the septal PG synthase that closes the septal annulus. Also unlike in rod-shaped bacteria, a Class A PBP moves processively at midcell, distinctly from components of the core PG elongasome or septal PG synthase. Thus, processive, circumferential motion in pneumococcal cells follows spatially separate linear tracks that may reflect a common ordered structure in the existing peptidoglycan itself. In contrast, the MpgA muramidase displays a different kind of subdiffusive motion that is largely confined to midcell by an unknown mechanism.

INTRODUCTION

The peptidoglycan (PG) cell wall protects bacteria from osmotic stress, determines cell shape, size, and chaining critical for adaptation and host interactions, and serves as a scaffolding in Gram-positive bacteria for the attachment of wall-teichoic acids, capsules, and extracellular enzymes and virulence factors (1-5). PG synthesis has provided targets for a large number of clinically relevant antibiotics and remains one of the most fertile sources for the discovery of new antibiotic targets in drug-resistant pathogens (6-11). Although a general picture of PG synthesis has emerged (12-16), many fundamental questions remain unanswered about the composition, coordination, chronology, and regulation of the nanomachines that carry out PG synthesis in bacteria. Moreover, major differences have recently emerged in how different bacteria carry out PG synthesis and

use homologous proteins in different ways (see (17-23)). *Streptococcus pneumoniae* (pneumococcus; *Spn*) has emerged as a model for PG synthesis in ovoid-shaped bacteria that is tractable to genetic, biochemical, and cell biological approaches (reviewed in (4, 24, 25)). *S. pneumoniae* is a human nasopharyngeal commensal bacterium that becomes a serious opportunistic pathogen, killing over one million people annually worldwide (26-28). Moreover, *S. pneumoniae* is an antibiotic-resistant "superbug," for which new antibiotic targets are urgently needed (10, 29-31).

Unlike in rod-shaped bacteria, all PG synthesis is zonal and confined to a band at the middle of dividing *S. pneumoniae* cells (Fig. S1) (24, 32, 33). At the start of cell division, the septal and elongation (peripheral) PG synthesis nanomachines locate to an FtsZ ring at the equators of predivisional daughter cells (Fig. S1*A*) (34, 35). Unlike *Bacillus subtilis* and *Staphylococcus aureus* (36-39), septal ring closure and cell separation occur simultaneously during the *S. pneumoniae* cell cycle, as do septal and elongation PG synthesis, with elongation PG synthesis likely starting slightly before septal PG synthesis in the initial FtsZ ring (24, 32, 33, 35, 40). As septation progresses, the septal and elongation PG synthesis nanomachines physically separate to the inside and outside edges, respectively, of the midcell annular disk (Fig. S1*B* and S1*C*) (24, 33, 41). Septal PG synthesis in the inner ring, which contains FtsZ and the Class B bPBP2x:FtsW (SEDS) complex, separates the dividing cells (24, 32-35). Elongation PG synthesis, which is carried out by the pneumococcal core elongasome in the outer ring (24, 32, 33), emanates outward and has been postulated to push MapZ-nascent FtsZ/FtsA/EzrA rings toward the equators of new daughter cells (Fig. S1*A*) (34, 42, 43). Notably, *S. pneumoniae* lacks Min and Noc systems (44, 45) and forms FtsZ rings over the nucleoid (22, 46, 47).

97 Consequently, dividing pneumococcal cells characteristically contain three FtsZ rings
98 throughout most of division, one at the closing septum and two in the developing
99 equatorial rings (Fig. S1*A*) (34, 46, 48). Interestingly, proteins that mediate bundling FtsZ
100 filaments, such as SepF, ZapA, and ZapJ (ZipA is absent), arrive to the equatorial rings
101 very late in cell division (34, 41, 49).

102 Septal ring closure is zonal and confined to a midcell ring in many bacteria (50-52).
103 Dynamics studies showed that the pneumococcal bPBP2x:FtsW PG septal synthase
104 moves circumferentially at midcell driven by PG synthesis itself, and not by FtsZ
105 treadmilling (34), as was initially concluded for *B. subtilis* (53). Recent papers
106 demonstrate that zonal septal closure is indeed driven by circumferential septal PG
107 synthesis in *Escherichia coli* (54), *S. aureus* (55), and *B. subtilis* (56), rather than by FtsZ
108 treadmilling.

109 However, elongation PG synthesis in rod-shaped cells is not zonal but is distributed
110 along the curved cylindrical body of growing cells (57-59). This synthesis is carried out by
111 the Rod-complex elongasome consisting of MreB and the PG elongasome complex.
112 Actin-like MreB polymerizes into multiple short, curved filaments perpendicular to the cell
113 long axis along the cell membrane, which is the region of maximal negative Gaussian
114 curvature (16, 60-62). MreB interacts with the cytoplasmic helix-turn-helix domain of the
115 bitopic RodZ protein that also interacts with the elongasome PG synthase complex facing
116 outside the cell membrane (62-65). The core elongasome consists of the polytopic shape,
117 elongation, division and sporulation (SEDS) family protein RodA (glycosyltransferase;
118 GT), an essential bitopic Class B bPBP (transpeptidase; TP), and bitopic and polytopic
119 positive regulators MreC and MreD, respectively (16, 66-70). Similar to septal PG

synthesis, movement of the assembled Rod elongasome is driven by side-wall PG synthesis itself, rather than by ATPase-dependent treadmilling of MreB (57-59). Thus, MreB filaments serve as curvature-sensing “rudders” for processive synthesis of separate parallel strands of side-wall PG (61). In addition, Class A PBPs, which are bitopic proteins with extracellular GT and TP activities, move largely in non-ordered paths and often stop, possibly filling in or reinforcing gaps left by the Rod system (16, 71-74).

In contrast to rod-shaped bacteria, pneumococcal elongasome PG synthesis is zonal and confined to the initial FtsZ ring and later to the outer edge of the septal annular disk (24, 32, 33). The core pneumococcal elongasome contains RodA, Class B bPBP2b, RodZ, MreC, and MreD, but does not contain an MreB homolog (19, 25, 35, 46, 75-79). RodZ(*Spn*) serves as an organizer of elongasome assembly and is required for MreC midcell localization followed by localization of RodA and bPBP2b (19, 80). Immunofluorescence microscopy (IFM) indicated that Class A aPBP1a and the MpgA muramidase co-localize with bPBP2b and MreC, but not with bPBP2x, throughout the cell cycle, including after the outer elongasome PG synthesis ring forms at midcell (Fig. S1) (35, 46, 80). Thus, aPBP1a and MpgA localize with peripheral PG synthesis, although it has not been determined whether they are persistent members of the core elongasome.

Paradoxically, the absence of aPBP1a suppresses the requirement for MreCD and RodZ (80, 81), whereas inactivation of *pbp1b*, which encodes Class A aPBP1b, suppresses the requirement for RodZ, but not for MreCD (19). In both cases, the bPBP2b:RodA PG synthase is still required for viability, suggesting that the absence of aPBP1a or aPBP1b may activate bypass pathways that obviate the requirement for certain regulators of the core elongasome (19, 80). However, amino acid changes that

143 reduce the catalytic activity of the MpgA muramidase (80, 82) abolish the requirement for
144 the entire pneumococcal PG elongasome, including the bPBP2b:RodA PG synthase (24,
145 80). The CozE protein was also implicated in pneumococcal elongation PG synthesis
146 (83). However, CozE did not behave equivalently to MreCD in transformation assays of
147 function (84), and the exact function of pneumococcal CozE remains unknown. A
148 pneumococcal TseB homolog renamed as CopD was recently reported to bind to bPBP2b
149 and aPBP1a. Absence of CopD produces wider cells, consistent with a defect in
150 elongation PG synthesis (85); however, the mechanism underlying this morphology
151 change is not known. Last, FtsX is located with the outer ring elongasome proteins later
152 in pneumococcal division (32). FtsX is a subunit of the FtsEX:PcsB PG hydrolase that is
153 thought to play an essential role in PG remodeling between septal and peripheral PG (86-
154 89). Notably, the FtsX(*Bsu*) homolog is also associated with side-wall PG synthesis (90,
155 91).

156 In this paper, we show that the pneumococcal bPBP2b, RodA, and MreC core
157 elongasome proteins move circumferentially with the same velocity and processivity at
158 midcell at different division stages. Unless indicated otherwise, midcell refers to the
159 central rings at the septa of dividing cells and to the equators of predivisional daughter
160 cells about to start division. The processive movement of the core elongasome
161 components is driven by PG synthesis, and is not affected by FtsZ treadmilling, consistent
162 with the absence of FtsZ in the outer ring of elongasome PG synthesis later in division.
163 Strikingly, at WT protein expression levels in exponentially growing cells, a large majority
164 of bPBP2b, RodA, and MreC molecules diffuse in the membrane over the body of
165 pneumococcal cells without synthesizing PG. Unexpectedly, Class A aPBP1a also moves

166 circumferentially at midcell with a similar velocity, but in shorter tracks, than the core
167 elongasome components. Processive movement of aPBP1a at midcell depended on PG
168 synthesis, and again, a majority of aPBP1a molecules were found diffusing over the cell
169 body without synthesizing PG. Finally, the MpgA muramidase showed a distinctive
170 pattern of non-processive, subdiffusive movement, largely confined to midcell regions.
171 These results demonstrate that the pneumococcal PG elongasome moves zonally, which
172 is different from elongasome movement in rod-shaped bacteria, that a Class A PBP
173 moves circumferentially as well as diffusively, and that a PG hydrolase shows unusual
174 fast non-processive movement confined largely to the midcell region. The implications of
175 these modes of movement to the functions of the pneumococcal PG elongasome, Class
176 A PBPs, and PG muramidases and to patterns of PG-glycan strand placement are
177 discussed.
178

179 **RESULTS**

180 **Construction of functional fluorescent-protein fusions.** Fusions to pneumococcal
181 elongasome proteins bPBP2b, RodA, MreC, aPBP1a, and MpgA, were constructed at
182 native chromosomal loci to contain an N-terminal expression-enhancing "i-tag", fused to
183 an intracellular HaloTag (HT) domain, followed by a 15 amino-acid linker, fused to the
184 protein of interest (Tables S1 and S2), as described previously (32, 34, 92-95). Growth of
185 strains expressing iHT-fused proteins in C+Y, pH 6.9 medium was indistinguishable from
186 that of WT (Fig. S2*A*). Localization of iHT-fused proteins labeled with saturating amounts
187 of HT-TMR ligand matched previously published localization patterns of epitope-tagged
188 or GFP-fused proteins imaged by IFM or two-dimensional epifluorescence microscopy

189 (2D-FM), respectively (Fig. S2*B*) (19, 32, 34, 35, 42, 46, 80, 81, 85, 96). Western blots of
190 these fusions with intracellular iHT domains probed with antibody to native MreC,
191 bPBP2b, aPBP1a, or MpgA showed expression of full-length fusions with minimal
192 cleavage of the iHT domain (Figs. S3*A*, S4*B*, S5*B* and S6). In contrast, western blots of
193 an extracellular C-terminal HT fusion to MreC (MreC-HT) probed with anti-MreC antibody
194 showed extensive cleavage of the HT domain not detectable in blots probed with anti-HT
195 antibody (Fig. S3*A*, middle and right). Cleavage of extracellular HT domains was also
196 reported in *E. coli* (97), and our results emphasize the need to validate protein fusion
197 stability in blots with antibody to native proteins.

198 We reported previously that some tagged proteins, such as iHT-bPBP2b and sfGFP-
199 bPBP2b, were expressed from their chromosomal locus in significantly lower amounts
200 than WT bPBP2b in cells grown in BHI broth, with only minor effects on cell growth and
201 morphology under this growth condition (32). We observed similar results for cells grown
202 in C+Y, pH 6.9 medium, which is required for live-cell fluorescence microscopy (34). The
203 cellular amounts of iHT-bPBP2b and iHT-aPBP1a were 15 ± 5% and 10 ± 10% (mean
204 ±SD) of the WT bPBP2b and aPBP1a amounts, respectively (Fig. S4*B* and S5*B*; Table
205 S3). Underproduced iHT-bPBP2b caused minor increases in cell width and size (Fig. S4
206 *C* and *D*). However, the reduced amount of iHT-aPBP1a partly phenocopied a Δ*pbp1a*
207 mutant (Fig. S5 *C* and *D*). The cellular amounts of iHT-MreC and iHT-MpgA expressed
208 from their chromosomal loci were 82 ±18% and 171 ± 11% of the WT MreC and MpgA
209 amounts, respectively (Figs. S3*A* and S6; Table S3). Cells expressing iHT-MreC showed
210 minimal cell morphology differences from WT (Figs. S2*B* and S3*B*).

211 To increase cellular amounts of iHT-bPBP2b, iHT-aPBP1a, and iHT-RodA (antibody
212 to native RodA was not available), we constructed merodiploid strains in which each iHT-
213 tagged protein was also expressed from an ectopic site under the control of a zinc-
214 inducible promoter (98). Addition of Zn inducer ([$ZnCl_2$] indicated + 1/10 [$MnSO_4$] to
215 reduce zinc toxicity (41, 80, 99)) to cultures of these merodiploid strains did not affect
216 growth (Figs. S4*A* and S5*A*). Zn addition complemented the low cellular amounts of iHT-
217 bPBP2b and iHT-aPBP1a back up to 82 ± 6% and 101 ± 41% of the WT bPBP2b and
218 aPBP1a amounts, respectively (Figs. S4*B* and S5*B*; Table S3). Complementation also
219 alleviated minor cell shape defects detected in strains with reduced protein amounts
220 (Figs. S4*C* and *D*, S5*C* and *D*, and S7). iHT-fused proteins localized strongly to midcell
221 of Zn-induced merodiploid strains, but were also more dispersed over bodies of cells
222 compared to haploid or uninduced merodiploid strains (Figs. S4*C* and S5*C*). Finally,
223 merodiploid strains expressing iHT-bPBP2b or iHT-RodA showed minimal amounts of
224 cleavage products when 0.2 mM or 0.25 mM Zn inducer was added to the growth medium
225 (Figs. S4*B* and S7*B*). Effects of protein amounts on dynamics are described below.

226 **bPBP2b, RodA, and MreC display similar processive circumferential motion at**
227 **midcell.** Strains expressing functional iHT-fused proteins were labeled with limiting
228 concentrations of HT-JF549 ligand (Table S4), and single-molecule total internal
229 reflection fluorescence microscopy (sm-TIRFm) was performed for 180 s, as described
230 previously (34) (*Materials and Methods*). Three criteria were used to determine different
231 motion types. Processive circumferential motion was defined as a molecule moving in
232 one direction for more than six consecutive frames (imaging rate = 1 frame per second
233 (FPS)), with a linear velocity of ≥ 5 nm/s determined by kymograph analysis (Fig. 1*A*;

234 *Materials and Methods*). Static molecules were defined as being visible for more than six
235 consecutive frames with a velocity < 5 nm/s. Diffusively moving molecules were defined
236 as moving, but not in a consistent direction, for 6 or more non-consecutive frames within
237 a period of 90 s.

238 Single molecules of iHT-bPBP2b, iHT-RodA, and iHT-MreC displayed similar
239 processive circumferential motion exclusively at midcell (Fig. 1*A* and S8 and Movies S1
240 to S3), that resembled the circumferential motion of iHT-bPBP2x and FtsW-HT reported
241 previously (34). The frequency of circumferential, static, and diffusive molecules was
242 compiled for each strain (Fig. 1*B*). Examination of the circumferential tracks showed that
243 73% (54/74) of iHT-bPBP2b and 74% (57/77) of iHT-MreC molecules moved
244 unidirectionally at midcell. The remaining 27% of iHT-bPBP2b or 26% of iHT-MreC
245 molecules moved in one direction for at least six consecutive frames and then reversed
246 direction and moved in the opposite direction for at least six frames at approximately the
247 same velocity (angle in kymograph; Fig. 1*A*, right). Slow or non-moving static molecules
248 were mainly detected at midcell (Fig. S8), whereas diffusive molecules displayed rapid,
249 erratic movement throughout the cell (Fig. 1*B* and S8 and Movies S1 to S3). Fewer than
250 5% of molecules of these core elongasome proteins were observed to transition between
251 movement states (e.g., static to diffusive or circumferential).

252 **A limited number of bPBP2b, RodA, and MreC molecules engage in active PG**
253 **synthesis.** The distribution of single-molecule movement states of iHT-bPBP2b and iHT-
254 RodA was highly dependent on cellular protein levels. When expressed at 15% of the WT
255 level, ≈60% of iHT-bPBP2b moved circumferentially and only 32% moved diffusively (Fig.
256 1*B* and Movie S1). The remaining 7% of iHT-bPBP2b molecules were static, mainly at

257 midcell. iHT-RodA molecules expressed from the native locus showed a similar
258 distribution, suggesting that iHT-RodA was underproduced (Fig. 1*B* and Movie S2).
259 However, when iHT-PBP2b and iHT-RodA protein amounts were increased by ectopic
260 expression (to ≈82% the WT level for iHT-bPBP2b), only 16% or 9% of single iHT-bPBP2b
261 or iHT-RodA molecules, respectively, moved circumferentially, while ≈70% moved
262 diffusively, with the remaining 12% iHT-bPBP2b or 23% iHT-RodA static, mostly at
263 midcell (Fig. 1*B* and Movies S4 and S5). Uninduced merodiploid strains expressing iHT-
264 bPBP2b or iHT-RodA displayed movement distributions similar to those of haploid strains
265 (Fig. 1*B*). The amount iHT-MreC expressed from its native locus was nearly (82%) that
266 of WT (Fig. S3*A* and Table S3). Approximately 24% of iHT-MreC molecules moved
267 circumferentially, while 52% moved diffusively and 24% were static, similar to the
268 movement distributions of iHT-bPBP2b and iHT-RodA when they were ectopically
269 expressed (Fig. 1*B* and Movie S3).

270 High-resolution 3D structured-illumination microscopy (3D-SIM) on fixed cells
271 corroborated conclusions based on movement distributions. At protein amounts
272 corresponding to ≈15% of WT, iHT-bPBP2b localized primarily to regions of active PG
273 synthesis at midcell and equators of dividing cells, as indicated by HADA fluorescent D-
274 amino-acid labeling (Fig. 2*A*). When expressed near the WT level, iHT-bPBP2b remained
275 at the HADA-labeled midcell and equators but was mostly dispersed over the body of the
276 entire cell where HADA labeling was not detected (Fig. 2*B*). These results support the
277 conclusion that iHT-PBP2b molecules that move diffusively in the cell membrane outside
278 of midcell and equators are not actively synthesizing PG (Fig. 2*B*). Control experiments
279 using a GFP fusion construct to bPBP2b and labeling with a different fluorescent D-amino

acid (TADA) gave similar results (Fig. S9). 2D-FM images also showed an increase in dispersed iHT-bPBP2b localization when protein expression was increased to near the WT amount (Fig. S4*C*). We conclude that at any given time, a limited number of bPBP2b, RodA, and MreC molecules display processive circumferential motion at midcell where PG synthesis occurs. Conversely, bPBP2b, RodA, and MreC are expressed in excess in WT cells, and most molecules are diffusing over the cell surface and not synthesizing PG in cells under these and other growth conditions (Figs. 1*B*, 2*B* and S4*C*; Table S3) (32).

bPBP2b, RodA, and MreC form a stable elongasome complex that undergoes circumferential motion. If bPBP2b, RodA, and MreC form an elongasome complex, we would expect that each molecule would move with the same velocity. To test this idea, velocities of circumferentially moving molecules were determined by kymograph analysis (Fig. 3*A*) (34). The length of time these molecules were observed moving circumferentially, referred to here as the circumferential duration, was also measured (Fig. 3*B*), and the particle distance each circumferential molecule moved was calculated by multiplying the velocity by the duration (Fig. S10*A*). When expressed near WT levels (+Zn in merodiploid and haploid *mreC* constructs) the mean circumferential velocities, durations, and particle distances of iHT-bPBP2b, iHT-RodA, and iHT-MreC were statistically the same, at ≈11 nm/s, ≈23 s, and ≈230 nm, respectively (Fig. 3*A* and *B*; Fig. S10*A*). Additional strains containing different fusion constructs of bPBP2b or RodA moved at similar circumferential velocities (Fig. S11). These data support the idea that bPBP2b, RodA, and MreC form a stable, circumferentially moving elongasome complex at midcell.

Circumferential movement of bPBP2b and RodA is independent of FtsZ treadmilling and driven by PG synthesis. Circumferential movement of the

303 pneumococcal septal PG synthase was shown to be independent of FtsZ treadmilling and
304 driven by PG synthesis {Perez, 2019 #136}. A similar conclusion was later reported for
305 the septal PG synthases of *S. aureus* (55) and *B. subtilis* (56) and for the population of
306 active septal PG synthases in *E. coli* (54, 100). In early divisional cells, the pneumococcal
307 PG elongasome is located in an FtsZ-ring that also contains the septal PG synthase (Fig.
308 S1*A*), whereas at later stages of division, the elongasome separates from the FtsZ-ring
309 and locates to the outer edge of the septal annular disk (Fig. S1 *B* and *C*) (24, 32, 33).
310 Notably, the same circumferential velocity of core elongasome protein iHT-MreC, which
311 was expressed near the WT level (Fig. S3*A*), was detected at equators of early divisional
312 cells, before ostensible constriction, and in later-divisional cells with clear constrictions,
313 when septal (inner) and elongasome (outer) rings are separated at midcell (32) (Figs.
314 S1*B* and S10*B*). Since the pneumococcal PG elongasome is initially in an FtsZ ring, we
315 tested whether iHT-bPBP2b velocity is decreased when FtsZ treadmilling is greatly
316 reduced by ectopic expression of GTPase mutant FtsZ(D214A), which reduces FtsZ
317 treadmilling velocity from ≈32 nm/s to ≈4 nm/s (34). To the contrary, overproduction of
318 FtsZ(D214A) caused a statistically minimal increase in iHT-bPBP2b velocity (Fig. 4*A* and
319 Movie S6), with a marginal decrease in growth rate (Fig. S12). Consistent with a lack of
320 dynamic coupling, the treadmilling velocity of FtsZ-sfGFP filaments was ≈2.4-fold greater
321 than the circumferential velocity of iHT-bPBP2b single molecules expressed in the same
322 cell (Fig. 4*B*; Movie S7). We conclude that circumferential movement of the
323 pneumococcal PG elongasome is independent of FtsZ treadmilling.

324 Two lines of evidence indicate that pneumococcal PG elongasome circumferential
325 movement is driven by PG synthesis. First, we determined iHT-bPBP2b or iHT-RodA

326 circumferential velocity in a Δ*murZ* (previously called Δ*murA1*) mutant, which lacks the
327 predominant MurZ homolog that catalyzes the first committed step of PG precursor
328 synthesis (34, 101). The circumferential velocity of iHT-bPBP2b or iHT-RodA was
329 substantially reduced by ≈1.6-fold in the Δ*murZ* mutant compared to WT (Fig. 4 *C* and *D*,
330 Movies S8 and S9). Previously, we showed that the velocity of FtsZ treadmilling is
331 unchanged in the Δ*murZ* mutant (34). Together, these results demonstrate that the rate
332 of midcell elongasome movement is dependent on PG synthesis precursor amounts.

333 Second, catalytic mutants of bPBP2b TP or RodA GT activity did not exhibit
334 processive, circumferential movement. No β-lactam antibiotic is known that preferentially
335 inhibits bPBP2b alone (102). Both bPBP2b and RodA are essential in *S. pneumoniae* (35,
336 75, 103). Consequently, we constructed merodiploid strains with *iht-pbp2b*(S391A) (TP
337 catalytic mutation) or *iht-rodA*(D283A) (GT catalytic mutation) (69) at chromosomal native
338 sites and *pbp2b*$^+$ or *rodA*$^+$ under the control of the zinc-inducible promoter (P_{Zn}) in an
339 ectopic site (Fig. 5*A*). The merodiploid strains were constructed and grown in the
340 presence of Zn inducer, which was removed to deplete the WT proteins (Fig. 5*B*).
341 Interestingly, we were able to construct a *rodA*(D283A)//P_{Zn}-*rodA*$^+$ strain, but we were
342 unable to construct a *pbp2b*(S391A)//P_{Zn}-*pbp2b*$^+$ strain in the presence of Zn inducer.
343 This result suggested that *pbp2b*(S391A) was dominant-negative to WT *pbp2b*$^+$. The
344 reason we were able to construct the *iht-pbp2b*(S391A)//P_{Zn}-*pbp2b*$^+$ merodiploid was the
345 low (≈15%) intrinsic expression of iHT-bPBP2b compared to WT bPBP2b (Fig. S4*B*).
346 Consistent with a dominant-negative effect, depletion of WT bPBP2b in the *iht-*
347 *pbp2b*(S391A)//P_{Zn}-*pbp2b*$^+$ merodiploid resulted in a more severe drop in OD_{620} than in
348 Δ*pbp2b*//P_{Zn}-*pbp2b*$^+$ (Fig. 5*B*), possibly due to the toxicity of uncrosslinked PG produced

349 from GT activity without TP activity (104). Western blot analysis confirmed that both iHT-
350 bPBP2b(S391A) and iHT-RodA(D283A) were expressed and stable relative to iHT-
351 bPBP2b$^+$ and iHT-RodA$^+$, respectively (Fig. S13*A*), and that bPBP2b$^+$ expressed from the
352 ectopic locus was fully depleted after 3h (Fig. S13*B*).

353 No midcell circumferential movement of iHT-bPBP2b(S391A) was detected in the
354 presence or absence of WT bPBP2b (Fig. 5*C*; Movies S10 and S11). Instead, iHT-
355 bPBP2b(S391A) was static at midcell (Fig. 5*D*) or was detected diffusing over the body
356 of cells (Fig. 5*C*). Likewise, no midcell circumferential movement of iHT-RodA(D283A)
357 was detected in the absence of RodA$^+$ (Fig. 5*C* and Movie S12). Like iHT-
358 bPBP2b(S391A), iHT-RodA(D283A) was static at midcell (Fig. 5*D*) or diffusing over the
359 body of cells (Fig. 5*C*). Notably, both iHT-bPBP2b(S391A) and iHT-RodA(D283A) located
360 to midcell (Fig. 5*E*), indicating that catalytic activity was not required for normal
361 localization. From these combined results, we conclude that processive, circumferential
362 movement of the pneumococcal elongasome PG synthase is driven by PG synthesis, but
363 not by FtsZ treadmilling, even in predivisional cells.

364 **bPBP2b localization becomes diffuse and circumferential movement is lost**
365 **when MreC is depleted.** We reported previously that the pneumococcal PG elongasome
366 is assembled sequentially (19). RodZ directs localization of MreC, which then directs
367 localization of the bPBP2b:RodA synthase. In agreement with this conclusion, iHT-
368 bPBP2b localization became diffuse when MreC was depleted (Fig. 6*A*). In addition, there
369 was a large (≈30-fold) drop in the number of iHT-bPBP2b molecules moving
370 circumferentially when MreC was depleted (Fig. 6*B* and Movie S13). Growth curve
371 analysis confirmed reduced growth yield of cells depleted for MreC (Fig. S14*A*), and

372 western blots confirmed the presence of iHT-bPBP2b during MreC depletion (Fig. S14 *B*
373 and *C*). We conclude that MreC is required for proper midcell localization and for
374 elongasome PG synthesis by the bPBP2b:RodA synthase. This result is consistent with
375 the previous conclusion that MreC allosterically activates the GT/TP activity of
376 RodA:PBP2 in the PG elongasome of *E. coli* (16, 67, 105).

377 **bPBP2b and RodA require each other for localization.** We further tested whether
378 RodA was required for bPBP2b localization, and *vice versa*. Indeed, upon RodA
379 depletion, iHT-bPBP2b went from locating primarily to midcell to being distributed at
380 midcell and over the surface of rounded cells (Figs. 7*A* and S15*C*), indicative of loss of
381 peripheral PG synthesis (35, 75, 81). Additionally, a growth yield phenotype was observed
382 at 4 to 5 h into depletion (Fig. S15 *A* and *B*). Upon bPBP2b depletion to ≈6% of WT after
383 3 h (Fig. S13*B*), iHT-RodA also relocated primarily from midcell to being distributed at
384 midcell and over the surface of rounded cells, with a similar reduction in growth yield
385 (Figs. 7*B* and S15). Therefore, there is an interdependence for normal localization of
386 bPBP2b and RodA in the pneumococcal PG elongasome.

387 We next determined the dynamics of iHT-bPBP2b upon depletion of RodA or iHT-
388 RodA upon depletion of bPBP2b. In both cases, the motion distribution shifted from
389 primarily circumferential (≈59%) to diffusive (≈65%) movement (Fig. 7*C*; Movies S14 and
390 S15), where iHT-bPBP2b and likely iHT-RodA were underproduced in these stains (Figs.
391 1*B,* S7 and S13*B*). Remaining circumferential movement at the midcell (≈24% of
392 molecules) likely reflected bPBP2b:RodA complexes that assembled before depletion
393 occurred. Consistent with this interpretation, the velocity of circumferentially moving
394 proteins was unchanged by depletion of its cognate partner (Fig. 7 *D* and *E*). These data

395 support the idea that when bPBP2b or RodA is depleted, its unpaired cognate partner
396 stops elongation PG synthesis at midcell and is released to diffuse over the cell body.
397 Notably, released, unpaired iHT-bPBP2b or iHT-RodA did not move circumferentially at
398 an increased velocity, suggesting that FtsZ filament end-tracking does not occur for these
399 proteins (100).

400 **aPBP1a displays circumferential dynamics at midcell driven by PG synthesis**
401 **but is not persistently part of the elongasome.** Molecules of iHT-aPBP1a
402 unexpectedly displayed circumferential, as well as diffusive and static dynamics (Fig. 1 *A*
403 and *B*; Movies S16 to S18). Like iHT-bPBP2b and likely iHT-RodA, iHT-aPBP1a was
404 underproduced in the haploid strain and required ectopic expression to reach or surpass
405 WT levels (Fig. 1*B* and Fig. S5*B*). However, in contrast to core elongasome components,
406 the relative frequency of circumferentially moving iHT-aPBP1a molecules (≈10%) was
407 largely independent of protein expression level (Fig. 1*B*), and a high percentage (>60%)
408 of iHT-aPBP1a molecules moved diffusively, even at low expression levels (Fig. 1*B*; Fig.
409 S5*B*; Table S3).

410 The mean circumferential velocity of iHT-aPBP1a expressed near WT levels was ≈15
411 nm/s, which was similar to, if not somewhat faster than, that of iHT-bPBP2b, iHT-RodA,
412 and iHT-MreC (≈11 nm/s) (Figs. 1*A* and 3*A*). Strikingly, the mean circumferential duration
413 of iHT-aPBP1a molecules was ≈10 s, more than two-fold shorter than that of iHT-bPBP2b,
414 iHT-RodA, or iHT-MreC (≈23 s) (Fig. 1*A* and 3*B*). Altogether, these results indicate that
415 circumferential motion of aPBP1a is distinct from that of bPBP2b, RodA, and MreC,
416 suggesting that aPBP1a is not persistently part of the core elongasome complex,
417 although shorter interactions are still possible.

418 To confirm that circumferential movement of iHT-aPBP1a molecules depends on PG
419 synthesis, we constructed an *iht-pbp1a*(S370A)//P_{Zn}-*iht-pbp1a*(S370A) merodiploid strain
420 expressing catalytically inactive (TP null) iHT-aPBP1a(S370A) from both the native site
421 and ectopic locus (Table S1). The growth rate of the catalytically inactive iHT-
422 aPBP1a(S370A) merodiploid strain was reduced slightly (≈1.3-fold) when Zn inducer was
423 added to the growth medium (Fig. S16*A*), but protein expression and localization were
424 comparable to that of iHT-aPBP1a merodiploid strains (Fig. S16 *B* and *C*).
425 Circumferential, diffusive, and static molecules were sorted by cellular location into
426 midcell or locations other than midcell (non-midcell) (Fig. 8). Circumferential movement
427 of iHT-aPBP1a decreased substantially from a relative frequency of ≈21% for iHT-
428 aPBP1a to a marginal ≈3% for iHT-aPBP1a(S370A) at midcell, with the remainder of
429 midcell iHT-aPBP1a or iHT-aPBP1a(S370A) molecules static (Fig. 8, Movie S19).
430 Essentially no circumferentially moving molecules of iHT-aPBP1a or iHT-
431 aPBP1a(S370A) were detected outside of midcell (Fig. 8). A similar conclusion was
432 reached when data from Fig. 1*B* was sorted into midcell or non-midcell locations (Fig.
433 S17*A*). Since no PG synthesis was detectable by FDAA labeling away from the midcell
434 (Figs. 2 and S9), and nearly all aPBP1a molecules away from midcell were moving
435 diffusively (Figs. 8 and S17*A*), this further suggests that diffusively moving aPBP1a were
436 not actively synthesizing PG in exponentially growing cells. Taken together, these data
437 indicate that circumferentially moving iHT-aPBP1a molecules are actively synthesizing
438 PG, while inactive molecules are either static at midcell or moving diffusively throughout
439 the cell. A similar conclusion was reached for elongasome proteins iHT-bPBP2b, iHT-
440 RodA, and iHT-MreC (Figs. 1*B* and 2).

441 Other data were consistent with aPBP1a not being a constant component of the PG
442 elongasome. Notably, the velocity of iHT-aPBP1a in a merodiploid *iht-pbp1a*//P_{Zn}-*iht-*
443 *pbp1a* Δ*murZ* strain was similar to that of iHT-aPBP1a in a *murZ*$^+$ merodiploid strain (Fig.
444 S17*B*, Movie S20). Growth rate, protein amount, localization and relative frequency of
445 circumferential molecules of iHT-aPBP1a were also similar in the Δ*murZ* mutant and
446 *murZ*$^+$ strain (Figs. S16 and S17*C*). Therefore, unlike iHT-bPBP2b and iHT-RodA (Fig. 4
447 *C* and *D*), the circumferential velocity of iHT-aPBP1a was not decreased when PG
448 precursor amounts were reduced. In addition, we tested whether the relative frequency
449 of circumferential iHT-aPBP1a was changed in a *mpgA*(Y488D) Δ*pbp2b* mutant, which
450 lacks the core PG elongasome (80, 82). Reduced catalytic activity of MpgA(Y488D)
451 bypasses the requirement for the PG elongasome, but *mpgA*(Y488D) Δ*pbp2b* mutations
452 are synthetically lethal with Δ*pbp1a* (80), possibly indicating that aPBP1a can substitute
453 for the PG elongasome. Consistent with this notion, iHT-aPBP1a dynamics were the
454 same in a *mpgA*(Y488D) Δ*pbp2b* merodiploid strain as in a WT strain (Fig. S17*C*, Movie
455 S21).

456 **MpgA displays subdiffusive movement restricted to midcell.** We investigated the
457 dynamics of iHT-MpgA (previously MltG(*Spn*)) muramidase, which has been genetically
458 linked to elongasome PG synthesis (80, 82). At an image acquisition rate of 1 FPS, the
459 majority of iHT-MpgA molecules (≈87%) appeared to move diffusively, but seemed to be
460 constrained mainly to the midcell region of cells (Fig. 1*B* and Movie S22), consistent with
461 a previous report that sfGFP-MpgA localizes at midcell (34). The remaining ≈13% of iHT-
462 MpgA molecules were static at midcell (Fig. 1*B*). There was also a small fraction (<1%)
463 of iHT-MpgA molecules that appeared to display rapid (>50 nm/s) movement of very short

464 duration at midcell (Figs. 3*A*, 3*B*, and 9*A*). However, this motion was difficult to track and
465 at the limit of the criterion used for continuous motion (six consecutive frames).

466 Consequently, we increased the data acquisition rate to 10 FPS. At this higher rate,
467 iHT-MpgA did not exhibit the processive, unidirectional movement observed for the
468 elongasome components and for aPBP1a (Figs. 1*A* and 9*B*). Instead, iHT-MpgA moved
469 erratically, mainly in the midcell region (see below; Fig. 9*B* and Movie S23). Measured at
470 10 FPS, the mean velocity of iHT-MpgA moving in short, directional stretches was
471 relatively fast (≈327 nm/s) compared to circumferential movement of other proteins (<20
472 nm/s), but slower than diffusing molecules in non-midcell regions (>1,000 nm/s) (Fig. 9*C*).
473 These distinctive subdiffusive dynamics did not support persistent association of MpgA
474 with the PG elongasome or aPBP1a during PG synthesis.

475 Given these unusual dynamics, we confirmed the functionality of the iHT-MpgA fusion
476 construct. The growth and cell morphology of strains expressing iHT-MpgA were similar
477 to those of WT, and iHT-MpgA showed expected midcell localization (Fig. S2). A mutant
478 expressing partially active MpgA(Y488D) suppressed the essentiality of the
479 pneumococcal PG elongasome in transformation assays (80). However, the *iht-mpgA*
480 construct failed to suppress Δ*pbp2b*, Δ*rodA*, Δ*mreC*, or Δ*rodZ* in transformation assays
481 (Table S5), indicating iHT-MpgA possessed muramidase activity. Unlike Δ*mpgA* mutants,
482 which accumulate suppressor mutations that inactivate aPBP1a (80); no *pbp1a* mutations
483 were detected in the *iht-mpgA* fusion strain by Sanger DNA sequencing. These results
484 indicated that the iHT-MpgA fusion protein was substantially active and that its dynamics
485 accurately reflected those of WT MpgA.

486 **Core PG elongasome components, aPBP1a, and MpgA display different**
487 **diffusion patterns.** We next investigated diffusion dynamics by performing sm-TIRFm at
488 20 FPS (*Materials and Methods*). Individual molecular trajectories were tracked (Fig. 10*A*)
489 and used to calculate mean-squared displacements (MSD) and diffusion coefficients (Fig.
490 10*B*) (106, 107). Diffusion coefficients were between 0.040 and 0.055 $\mu m^2/s$, comparable
491 to values determined previously for PG synthesis proteins in *S. pneumoniae*, *E. coli* and
492 *B. subtilis* (56, 100, 108, 109). Consistent with sm-TIRFm imaging at 1 FPS (Fig. 1*B*),
493 single molecules displayed rapid diffusive motion in non-midcell regions and much slower,
494 processive motion at midcell, where static molecules were also observed (Fig. 10*A* and
495 Movies S24 to S30). MSD curves generated for diffusively moving molecules were not
496 linear and plateaued as time increased, with alpha values <1, which is indicative of some
497 form of subdiffusion (Fig. 10*B*). Subdiffusion is commonly due to diffusion within a
498 confined space, but can also be caused by membrane crowding or interactions with other
499 molecules (110). For bacterial membrane proteins, this confined space is often the
500 surface area of the cell membrane (110).

501 Single-molecule trajectories of diffusively moving PG elongasome core components
502 iHT-bPBP2b, iHT-RodA, and iHT-MreC covered most of the cell area, while non-diffusive
503 processive and static molecules located to midcell, where active PG synthesis occurred
504 (Fig. 10*A* and Movies S24 to S26), consistent with results acquired at 1 FPS (Fig. S8).
505 This suggests that the subdiffusive behavior of the core elongasome proteins was due to
506 confinement within the cell membrane. The diffusion coefficients of iHT-bPBP2b and iHT-
507 MreC were similar (≈0.046 $\mu m^2/s$), and the MSD curves of diffusively moving molecules
508 plateaued in the same range (≈0.07 μm^2), indicating that iHT-bPBP2b and iHT-MreC

509 molecules were confined to a similarly sized area (Fig. 10*B*) (111). By contrast, iHT-RodA
510 had a slightly higher diffusion coefficient (0.050 $\mu m^2/s$) with a higher MSD curve plateau
511 (≈0.08 μm^2). These data suggest that bPBP2b and MreC may diffuse as a complex
512 through the membrane separately from RodA. Additional experiments are needed to test
513 this idea.

514 Diffusively moving iHT-aPBP1a molecules had an even greater diffusion coefficient
515 (≈0.055 $\mu m^2/s$) than those of the core components of the PG elongasome (Fig. 10*B*). iHT-
516 aPBP1a molecules also had a higher plateau in MSD plots (≈0.1 μm^2), indicative of
517 diffusive movement that was observed over the whole cell (Fig. 10*A* and Movie S27).
518 Again, non-diffusive, processively moving and static iHT-aPBP1a molecules were mostly
519 confined to midcell (Fig. 10*A*), as was observed by sm-TIRFm at 1 FPS (Fig. 8 and S17*A*).
520 Interestingly, we also observed some diffusive iHT-aPBP1a molecules that stopped
521 moving, paused for a short time (<1 s), and then resumed diffusive movement (Movie
522 S28). This pausing behavior was not readily detectable for diffusing components of the
523 PG elongasome. We conclude that diffusing aPBP1a molecules move differently from
524 components of the core PG elongasome in pneumococcal cells and that there is an
525 intermediate paused state during diffusion of aPBP1a.

526 Finally, diffusion analysis confirmed the unusual pattern of confined movement of iHT-
527 MpgA molecules at midcell. Unlike iHT-bPBP2b, iHT-RodA, iHT-MreC, and iHT-aPBP1a,
528 the majority of iHT-MpgA molecules did not diffuse over the whole cell but were largely
529 confined to midcell (Fig. 10*A* and Movie S29). This conclusion was further corroborated
530 by manually counting the location of iHT-MpgA tracks from data in Figure 10A. This
531 analysis showed that 74% (148/200) of the tracks of subdiffusive iHT-MpgA tracks were

532 located within 125 nm of midcell septa or equatorial rings. This confinement is likely
533 reflected by the low plateau (≈0.05 μm^2) in the MSD plot. In addition, the diffusion
534 coefficient (≈0.04 $\mu m^2/s$) of iHT-MpgA was considerably lower than those of the other
535 proteins that diffused over the body of cells (Fig. 10*B*), consistent with the sm-TIRFm
536 measurements at 10 FPS (Fig. 9). Similar to iHT-aPBP1a, iHT-MpgA subdiffusive
537 molecules were observed transitioning between diffusive motion and paused states
538 (Movie S30). Together, these results indicate that the confined, subdiffusive movement
539 of MpgA molecules is fundamentally different from that of components of the
540 pneumococcal core PG elongasome.
541

542 **DISCUSSION**

543 This paper shows that the core PG elongasome moves circumferentially around the
544 midcell of dividing *S. pneumoniae* cells (Fig. 1). The velocity of core elongasome
545 members bPBP2b, RodA, and MreC was statistically the same (≈11 nm/sec) (Fig. 3),
546 which is slightly slower than the velocity of the bPBP2x and FtsW (≈20 nm/sec)
547 components of the septal PG synthase (34). The processive motion of elongasome
548 members was driven by PG synthesis and was independent of FtsZ treadmilling (Fig. 4
549 and 5), and this motion was not dependent on stage of cell division (Fig. S10*B*). Strikingly,
550 the majority of bPBP2b or RodA molecules moved circumferentially in cells that severely
551 underproduced bPBP2b (≈15% of WT) or likely RodA (Fig. 1*B*). In contrast, in cells
552 expressing nearly WT protein levels, a minority of bPBP2b, RodA, and MreC molecules
553 either moved circumferentially and synthesized PG at midcell or exhibited nonmoving
554 static behavior at midcell (Fig. 1*B* and S8). The majority of core elongasome components

555 moved diffusively in the membrane over cell bodies, where PG synthesis was not
556 detected by FDAA labeling of exponentially growing cells (Fig. 2 and S9).

557 These observations indicate that pneumococcal elongation PG synthesis results from
558 processive, circumferential movement of PG elongasomes that are confined to a narrow
559 zone at midcell (Fig. 11). This pattern contrasts with the elongasome movement guided
560 by short MreB filaments and driven by PG synthesis that occurs over the body of many
561 rod-shaped bacteria (16). MreB-guided PG synthesis results in a dense mesh of
562 concentrically oriented PG glycan strands along the inner, sidewall surface of *B. subtilis*
563 cells (112). The circumferential movement of the pneumococcal PG elongasome
564 anticipates that peripheral PG glycan strands may likewise be concentrically aligned in *S.*
565 *pneumoniae* cells. These observations also indicate that in exponentially growing WT
566 cells, the core elongasome components are present in excess, with only a minority of
567 bPBP2b, RodA, and MreC engaged in active PG synthesis at midcell rings (Fig. 2 and
568 S9).

569 The results presented here further raise the issue of what directs circumferential
570 movement of elongasome components in tracks at midcell. The velocity of elongasome
571 components was not changed when treadmilling was greatly impeded in an *ftsZ*(GTPase)
572 mutant (Fig. 4*A*). Independence of FtsZ treadmilling fits the observation that FtsZ was not
573 detected in the outer midcell ring where peripheral PG synthesis occurs later in division
574 (Fig. S1*B*) (32). The similar velocity of MreC in predivisional cells when elongasomes are
575 still located in the FtsZ-ring as in later-divisional cells when the elongasome is in outer
576 midcell ring (Fig. S10*B*) is also consistent with independence of FtsZ treadmilling. In
577 addition, when RodA or bPBP2b was depleted, no unassociated bPBP2b or RodA was

578 detected being driven at the rate of treadmilling FtsZ (≈34 nm/sec; Fig 7 *D* and *E*), as
579 occurs for components of the septal PG synthase of *E. coli* (100). Moreover, a severe
580 decrease in FtsZ treadmilling speed led to only a marginal (≈17%) decrease in the speed
581 of the septal PG synthase in *S. pneumoniae* (34) and no decrease in *S. aureus* (55). In
582 *B. subtilis*, a slightly greater decrease (≈40%) in the speed of the septal PG synthase
583 when FtsZ treadmilling was moderately or greatly reduced has recently been attributed
584 to indirect effects (56). Thus, all evidence supports the conclusion that the movement and
585 speed of the septal and elongasome PG synthases in WT *S. pneumoniae* cells are driven
586 by PG synthesis, independent of FtsZ treadmilling.

587 It remains unknown what determines the tracks for the movement of the
588 pneumococcal septal or elongasome PG synthases in the inner and outer midcell rings,
589 respectively (Fig. S1). The muropeptide-crosslinked PG glycan strands to which new PG
590 is added may provide a rigid structure that directs processive PG synthesis in a linear
591 direction. Moreover, there appears to be a limited number of available sites in midcell
592 rings for septal and elongasome PG synthases to load and synthesize PG. As noted
593 above, only a minority of elongasome components are engaged in PG synthesis in WT
594 cells (Fig. 1*B*, 2, and 11). However, when the cellular amount of bPBP2b was reduced to
595 ≈15% of the WT level, the majority of bPBP2b molecules moved processively to
596 synthesize PG (Fig. 1*B*), consistent with a limited number of spots on rings for active PG
597 synthase complexes. Interestingly, ≈26% of circumferentially moving bPBP2b or MreC
598 molecules reversed direction within the timeframe of these experiments. Direction
599 reversal was also reported for processively moving members of the septal PG synthases
600 of *S. aureus* (55) and *B. subtilis* (113). This directional transitioning may be indicative of

601 PG synthase complexes stopping and reinitiating synthesis of a new glycan strand in the
602 opposite direction (55, 113).

603 We also observed nonmoving, static molecules of bPBP2b, RodA, and MreC
604 expressed at WT concentrations, primarily at midcell and to a lesser (≈5-fold) extent
605 elsewhere in cells (Fig. 1*B* and S8). When elongasome PG synthesis was halted by
606 expression of catalytically inactive proteins, circumferential movement also stopped and
607 molecules became static (Fig. 5*C* and 5*D*; Fig. 8) (69). To our knowledge, there is no
608 direct evidence that PBPs static for several seconds are actively synthesizing PG, as
609 suggested for aPBPs in *E. coli* (71, 74). To the contrary, when PG synthases stop
610 synthesis, they stop moving (Fig. 5 *C* and *D*; Fig. 8) (34, 55, 56, 114). Therefore, we think
611 it more likely that static PG synthases at midcell in WT cells may be incompletely
612 assembled complexes or complexes waiting to assume an available site for PG synthesis,
613 possibly stabilized by noncovalent binding of PBP TP domains to acceptor peptides in
614 PG (56, 109). Consistent with this idea, we observed transitions of MreC molecules from
615 the processive to static states (<5%), and *vice versa* (<1%). Outside of midcell, diffusion
616 analysis showed that inactive bPBP2b and MreC may diffuse together as a complex over
617 the cell body, while RodA diffuses separately (Fig. 10*B*). The mechanisms that arrange
618 and limit the number of active pneumococcal PG elongasomes remain to be determined.

619 The processive movement of pneumococcal Class A aPBP1a strikingly contrasts with
620 the diffusive motion for Class A PBPs reported previously in *E. coli* and *B. subtilis* (71,
621 74). Earlier IFM studies colocalized aPBP1a with elongasome components bPBP2b and
622 MreC (35). Instead of diffusive motion, aPBP1a molecules at midcell moved
623 circumferentially or were static (Fig. 8 and S17), and processive movement was abolished

624 in a *pbp1a*(TP) mutant (Fig. 8). Processively moving aPBP1a also reversed direction
625 infrequently (<9%). However, several results indicate that aPBP1a is not a persistent
626 member of the core PG elongasome. The duration of aPBP1a processive motion was
627 considerably shorter (≈10 s) than that of the PG elongasome components (≈23 s) (Fig.
628 3*B*). In addition, the relative frequency of circumferential motion of aPBP1a was
629 unchanged in a suppressed Δ*pbp2b mpgA*(Y488D) mutant that lacks an intact PG
630 elongasome (Fig. S17*C*). Like iHT-bPBP2b, iHT-aPBP1a was underproduced (10% of
631 WT) when expressed from its native chromosomal locus (Figs. 1*B* and S5*B*). But, unlike
632 iHT-bPBP2b, circumferentially moving aPBP1a was not the majority species at the low
633 expression level (Fig. 1*B*). In addition, unlike bPBP2b and RodA, aPBP1a processive
634 motion was not decreased in a Δ*murZ* mutant (Fig. S17 *B* and *C*), which may reflect a
635 different kinetic dependence for Lipid II substrate. Outside of midcell, aPBP1a moved
636 diffusively in the membrane over the whole length of cells (Figs. 8 and 10*A*). Together,
637 these results indicate that aPBP1a is not a persistent member of the pneumococcal core
638 PG elongasome (85), although shorter or transient interactions are possible (Fig. 11).

639 aPBPs have been proposed to play roles in normal PG synthesis and in repair of
640 damaged PG (1, 39, 73, 115). In rod-shaped bacteria, it was postulated that when
641 diffusing aPBPs encounter damaged PG, they cease moving and become static for
642 relatively long times (≈5 s) (71, 74). For reasons discussed above, long static PG
643 synthases may not be synthesizing PG. We also detected another aPBP1a motion away
644 from midcell in exponentially growing cells. Diffusing aPBP1a molecules infrequently
645 paused for short (<1 s) intervals, before resuming diffusive motion (Movie S28). It remains

646 to be determined whether static or paused aPBP1a molecules are repairing damaged PG
647 in *S. pneumoniae* cells.

648 In Gram-positive bacteria, the PG in the septal annular disk has a core of concentric
649 ordered PG glycan strands covered by a dense mesh of randomly oriented PG strands
650 that face the cell membrane (112). It has been postulated that aPBPs may synthesize this
651 layer of randomly oriented, inner-facing PG strands (39), although remodeling by PG
652 hydrolases followed by resynthesis could potentially contribute to this disordered pattern.
653 Circumferential, processive movement suggests that aPBP1a synthesis may result in
654 concentric, ordered PG glycan strands, rather than randomly oriented strands. Glycan
655 strands synthesized by the shorter tracks of aPBP1a motion are presumably shorter than
656 those synthesized by the more processive core PG elongasome. These shorter strands
657 may be remodeled and crosslinked into the longer strands to provide additional strength
658 to the peripheral PG layer. The dynamics of the other pneumococcal Class A PBPs,
659 aPBP2a and aPBP1b, remains to be determined. The circumferential movement of an
660 aPBP potentially has another implication to bacteria that elongate only from their poles,
661 such as *Rhizobiales* species, including *Agrobacterium tumefaciens* (116, 117). Polar
662 elongasome complexes in these bacteria lack bPBP:SEDS PG synthases, and PG
663 elongation is carried out only by a single essential aPBP (116, 117), which may move
664 circumferentially during PG elongation.

665 Finally, the subdiffusional, confined motion of the MpgA muramidase at midcell was
666 unexpected. IFM showed that MpgA (formerly MltG(*Spn*)), like aPBP1a, colocalized with
667 MreC to the outer ring in later-divisional cells (80). MpgA is an essential muramidase that
668 cleaves newly synthesized PG glycan chains 7 disaccharides from the undecaprenol

669 membrane anchor (82). A LysM domain in MpgA correctly places the cleavage point in
670 the glycan chain. Therefore, MpgA is thought to act as a PG release factor that frees
671 newly synthesized PG for crosslinking into existing PG (82). Instead of moving
672 circumferentially, most MpgA molecules moved at subdiffusion speeds (≈300 nm/sec)
673 that were slower than that of freely diffusing MpgA (>1,000 nm/sec). However, instead of
674 moving over the whole body of cells, MpgA molecules were largely confined to regions of
675 PG synthesis at midcell (Figs. 1*B* and 10*A*). Therefore, MpgA functions separately from
676 the core PG elongasome and from aPBP1a (Fig. 11). Only a fraction (≈13%) of MpgA
677 molecules were static, and we detected subdiffusing MpgA molecules that paused (<1 s)
678 and then resumed movement (Movie S30), similar to aPBP1a. Whether static or paused
679 MpgA are carrying out PG strand cleavage requires further study. Likewise, proteins that
680 interact with and regulate MpgA activity (118) and the mechanism that confines MpgA
681 movement to midcell await discovery.
682

683 **MATERIALS AND METHODS**

684 Bacterial strains used were unencapsulated (Δ*cps*) derivatives of *Streptococcus*
685 *pneumoniae* (*Spn*) serotype 2 strain D39W and are listed in Table S1. IU1945 and IU1824
686 were used as parent strains (Table S1). Detailed methods are described in *SI Appendix,*
687 *Materials and Methods*, including: bacterial strain construction and growth conditions;
688 ectopic expression and depletion conditions; cell labeling with HaloTag ligand; 2D-
689 epifluorescence microscopy and analysis; sm-TIRFm sample preparation; sm-TIRFm
690 imaging; sm-TIRFm image analysis; single-molecule tracking and diffusion analysis; 3D-

691 structured illumination microscopy and analysis; quantitative western blotting;
692 transformation assay.
693

694 **ACKNOWLEDGEMENTS**

695 We thank laboratory members and Jie Xiao (Johns Hopkins) for discussions about this
696 work; John D. Richardson and Ziyun A. Ye for technical assistance with some
697 experiments, Jim Powers (Indiana University Bloomington) for advice about light
698 microscopy; Mike VanNieuwenhze (Indiana University Bloomington) for FDAA reagents;
699 Luke Lavis (Janelia Lab) for Fluor JF549; Reinhold Brückner, and Regine Hakenbeck
700 (Kaiserlautern University) for anti-bPBP2x antibody; and Suzanne Walker and David Z.
701 Rudner (Harvard Medical School) for antibodies against pneumococcal PG synthesis
702 proteins. This work was supported by NIH grant R35GM131767 (to MEW), NSF grant
703 MCB1027504 (to SLS); NIH grant RO1AI148752 (to Suzanne Walker); NIH grant T32
704 GM109825 (to AJP); NIH grant F31AI138430 (to MML); NIH grants T32 GM007753 and
705 F30 AI156972 (to JEP), and NIH equipment grant S10OD024988 to the Indiana University
706 Bloomington (IUB) Light Microscopy Imaging Center.
707

708 **CONFLICT OF INTEREST**

709 The authors declare that they have no conflicts of interests.
710

711 **AUTHOR CONTRIBUTIONS**

712 AJP, MML, KEB, SLS, and MEW contributed to the conception or design of this study.
713 AJP, MML, KEB, MAT, JEP SLS, HCTT, and MEW contributed to the acquisition,

714 analysis, and interpretation of the data. KEB, HCTT, and MEW contributed to the writing
715 of the manuscript with input from the other authors.
716

717 **DATA AVAILABILITY**

718 The data that support the findings of this study are presented in the paper, including the
719 Supplemental Information and Appendix A.
720

721 **ORCID**

722 Amilcar J. Perez https://orcid.org/0000-0001-6729-7564
723 Melissa M. Lamanna https://orcid.org/0000-0002-6535-7903
724 Kevin E. Bruce https://orcid.org/0009-0005-3300-8863
725 Julia E. Page https://orcid.org/0000-0002-9884-2382
726 Sidney L. Shaw https://orcid.org/0000-0001-9195-6128
727 Ho-Ching T. Tsui https://orcid.org/0000-0003-0849-874X
728 Malcolm E. Winkler https://orcid.org/0000-0002-1482-2588
729

730 **REFERENCES**

731 1. E. A. Mueller, P. A. Levin, Bacterial Cell Wall Quality Control during Environmental
732 Stress. *mBio* **11** (2020).
733 2. M. Rajagopal, S. Walker, Envelope Structures of Gram-Positive Bacteria. *Curr Top*
734 *Microbiol Immunol* **404**, 1-44 (2017).
735 3. E. R. Rojas, The Mechanical Properties of Bacteria and Why they Matter. *Adv Exp*
736 *Med Biol* **1267**, 1-14 (2020).
737 4. W. Vollmer, O. Massidda, A. Tomasz, The Cell Wall of Streptococcus pneumoniae.
738 *Microbiol Spectr* **7** (2019).
739 5. K. D. Young, Bacterial shape: two-dimensional questions and possibilities. *Annu*
740 *Rev Microbiol* **64**, 223-240 (2010).
741 6. K. Bush, P. A. Bradford, Interplay between beta-lactamases and new beta-
742 lactamase inhibitors. *Nat Rev Microbiol* **17**, 295-306 (2019).

7. T. den Blaauwen, J. M. Andreu, O. Monasterio, Bacterial cell division proteins as antibiotic targets. *Bioorg Chem* **55**, 27-38 (2014).
8. K. Lewis, The Science of Antibiotic Discovery. *Cell* **181**, 29-45 (2020).
9. L. L. Ling *et al.*, A new antibiotic kills pathogens without detectable resistance. *Nature* **517**, 455-459 (2015).
10. L. T. Sham, H. C. Tsui, A. D. Land, S. M. Barendt, M. E. Winkler, Recent advances in pneumococcal peptidoglycan biosynthesis suggest new vaccine and antimicrobial targets. *Curr Opin Microbiol* **15**, 194-203 (2012).
11. J. Zhou *et al.*, Breaking down the cell wall: Still an attractive antibacterial strategy. *Front Microbiol* **13**, 952633 (2022).
12. S. Booth, R. J. Lewis, Structural basis for the coordination of cell division with the synthesis of the bacterial cell envelope. *Protein Sci* **28**, 2042-2054 (2019).
13. A. J. F. Egan, J. Errington, W. Vollmer, Regulation of peptidoglycan synthesis and remodelling. *Nat Rev Microbiol* **18**, 446-460 (2020).
14. S. Garde, P. K. Chodisetti, M. Reddy, Peptidoglycan: Structure, Synthesis, and Regulation. *EcoSal Plus* **9** (2021).
15. S. Kumar, A. Mollo, D. Kahne, N. Ruiz, The Bacterial Cell Wall: From Lipid II Flipping to Polymerization. *Chem Rev* **122**, 8884-8910 (2022).
16. P. D. A. Rohs, T. G. Bernhardt, Growth and Division of the Peptidoglycan Matrix. *Annu Rev Microbiol* **75**, 315-336 (2021).
17. C. Billaudeau *et al.*, Contrasting mechanisms of growth in two model rod-shaped bacteria. *Nat Commun* **8**, 15370 (2017).
18. P. J. Eswara, K. S. Ramamurthi, Bacterial Cell Division: Nonmodels Poised to Take the Spotlight. *Annu Rev Microbiol* **71**, 393-411 (2017).
19. M. M. Lamanna *et al.*, Roles of RodZ and class A PBP1b in the assembly and regulation of the peripheral peptidoglycan elongasome in ovoid-shaped cells of Streptococcus pneumoniae D39. *Mol Microbiol* **118**, 336-368 (2022).
20. S. P. Ouellette, J. Lee, J. V. Cox, Division without Binary Fission: Cell Division in the FtsZ-Less Chlamydia. *J Bacteriol* **202** (2020).
21. A. R. Pereira *et al.*, FtsZ-Dependent Elongation of a Coccoid Bacterium. *mBio* **7** (2016).
22. M. G. Pinho, M. Kjos, J. W. Veening, How to get (a)round: mechanisms controlling growth and division of coccoid bacteria. *Nat Rev Microbiol* **11**, 601-614 (2013).
23. A. M. Randich, Y. V. Brun, Molecular mechanisms for the evolution of bacterial morphologies and growth modes. *Front Microbiol* **6**, 580 (2015).
24. N. S. Briggs, K. E. Bruce, S. Naskar, M. E. Winkler, D. I. Roper, The Pneumococcal Divisome: Dynamic Control of Streptococcus pneumoniae Cell Division. *Front Microbiol* **12**, 737396 (2021).
25. O. Massidda, L. Novakova, W. Vollmer, From models to pathogens: how much have we learned about Streptococcus pneumoniae cell division? *Environ Microbiol* **15**, 3133-3157 (2013).
26. M. J. Cox, N. Loman, D. Bogaert, J. O'Grady, Co-infections: potentially lethal and unexplored in COVID-19. *Lancet Microbe* **1**, e11 (2020).
27. V. Sender, K. Hentrich, B. Henriques-Normark, Virus-Induced Changes of the Respiratory Tract Environment Promote Secondary Infections With Streptococcus pneumoniae. *Front Cell Infect Microbiol* **11**, 643326 (2021).

28. J. N. Weiser, D. M. Ferreira, J. C. Paton, Streptococcus pneumoniae: transmission, colonization and invasion. *Nat Rev Microbiol* **16**, 355-367 (2018).
29. CDC (2019) Antibiotic resistance threats in the United States, 2019. in *AR Threats Rep., U.S. Dep. Health Hum. Serv., Cent. Dis. Control Prev.* (AR Threats Report, U.S.A. Dept Health and Human Services, Center for Disease Control and Prevention, Atlanta, GA).
30. P. S. Gibson, J. W. Veening, Gaps in the wall: understanding cell wall biology to tackle amoxicillin resistance in Streptococcus pneumoniae. *Curr Opin Microbiol* **72**, 102261 (2023).
31. WHO (2017) List of bacteria for which new antibiotics are urgently needed. (World Health Organization, Geneva, Switzerland).
32. A. J. Perez *et al.*, Organization of peptidoglycan synthesis in nodes and separate rings at different stages of cell division of Streptococcus pneumoniae. *Mol Microbiol* **115**, 1152-1169 (2021).
33. J. Trouve *et al.*, Nanoscale dynamics of peptidoglycan assembly during the cell cycle of Streptococcus pneumoniae. *Curr Biol* **31**, 2844-2856 e2846 (2021).
34. A. J. Perez *et al.*, Movement dynamics of divisome proteins and PBP2x:FtsW in cells of Streptococcus pneumoniae. *Proc Natl Acad Sci U S A* **116**, 3211-3220 (2019).
35. H. T. Tsui *et al.*, Pbp2x localizes separately from Pbp2b and other peptidoglycan synthesis proteins during later stages of cell division of Streptococcus pneumoniae D39. *Mol Microbiol* **94**, 21-40 (2014).
36. J. Errington, L. J. Wu, Cell Cycle Machinery in Bacillus subtilis. *Subcell Biochem* **84**, 67-101 (2017).
37. V. A. Lund *et al.*, Molecular coordination of Staphylococcus aureus cell division. *Elife* **7** (2018).
38. B. M. Saraiva *et al.*, Reassessment of the distinctive geometry of Staphylococcus aureus cell division. *Nat Commun* **11**, 4097 (2020).
39. D. Straume, K. W. Piechowiak, M. Kjos, L. S. Havarstein, Class A PBPs: It is time to rethink traditional paradigms. *Mol Microbiol* **116**, 41-52 (2021).
40. R. Wheeler, S. Mesnage, I. G. Boneca, J. K. Hobbs, S. J. Foster, Super-resolution microscopy reveals cell wall dynamics and peptidoglycan architecture in ovococcal bacteria. *Mol Microbiol* **82**, 1096-1109 (2011).
41. A. J. Perez *et al.*, FtsZ-Ring Regulation and Cell Division Are Mediated by Essential EzrA and Accessory Proteins ZapA and ZapJ in Streptococcus pneumoniae. *Front Microbiol* **12**, 780864 (2021).
42. A. Fleurie *et al.*, MapZ marks the division sites and positions FtsZ rings in Streptococcus pneumoniae. *Nature* **516**, 259-262 (2014).
43. N. Holeckova *et al.*, LocZ is a new cell division protein involved in proper septum placement in Streptococcus pneumoniae. *mBio* **6**, e01700-01714 (2014).
44. V. W. Rowlett, W. Margolin, The Min system and other nucleoid-independent regulators of Z ring positioning. *Front Microbiol* **6**, 478 (2015).
45. L. J. Wu, J. Errington, Nucleoid occlusion and bacterial cell division. *Nat Rev Microbiol* **10**, 8-12 (2011).
46. A. D. Land *et al.*, Requirement of essential Pbp2x and GpsB for septal ring closure in Streptococcus pneumoniae D39. *Mol Microbiol* **90**, 939-955 (2013).

47. R. van Raaphorst, M. Kjos, J. W. Veening, Chromosome segregation drives division site selection in Streptococcus pneumoniae. *Proc Natl Acad Sci U S A* **114**, E5959-E5968 (2017).
48. M. Jacq *et al.*, Remodeling of the Z-Ring Nanostructure during the Streptococcus pneumoniae Cell Cycle Revealed by Photoactivated Localization Microscopy. *mBio* **6** (2015).
49. A. Mura *et al.*, Roles of the Essential Protein FtsA in Cell Growth and Division in Streptococcus pneumoniae. *J Bacteriol* **199** (2017).
50. P. A. Levin, A. Janakiraman, Localization, Assembly, and Activation of the Escherichia coli Cell Division Machinery. *EcoSal Plus* **9**, eESP00222021 (2021).
51. C. R. Mahone, E. D. Goley, Bacterial cell division at a glance. *J Cell Sci* **133** (2020).
52. L. M. Y. Mertens, T. den Blaauwen, Optimising expression of the large dynamic range FRET pair mNeonGreen and superfolder mTurquoise2(ox) for use in the Escherichia coli cytoplasm. *Sci Rep* **12**, 17977 (2022).
53. A. W. Bisson-Filho *et al.*, Treadmilling by FtsZ filaments drives peptidoglycan synthesis and bacterial cell division. *Science* **355**, 739-743 (2017).
54. X. Yang *et al.*, A two-track model for the spatiotemporal coordination of bacterial septal cell wall synthesis revealed by single-molecule imaging of FtsW. *Nat Microbiol* **6**, 584-593 (2021).
55. S. Schäper *et al.*, Processive movement of Staphylococcus aureus essential septal peptidoglycan synthases is independent of FtsZ treadmilling and drives cell constriction. *bioRxiv* 10.1101/2023.06.29.547026 (2023).
56. K. D. Whitley, J. Grimshaw, E. Karinou, P. J. Stansfeld, S. Holden, A one-track model for spatiotemporal coordination of Bacillus subtilis septal cell wall synthesis. *bioRxiv* 10.1101/2023.06.29.547024, 2023.2006.2029.547024 (2023).
57. J. Dominguez-Escobar *et al.*, Processive movement of MreB-associated cell wall biosynthetic complexes in bacteria. *Science* **333**, 225-228 (2011).
58. E. C. Garner *et al.*, Coupled, circumferential motions of the cell wall synthesis machinery and MreB filaments in B. subtilis. *Science* **333**, 222-225 (2011).
59. S. van Teeffelen *et al.*, The bacterial actin MreB rotates, and rotation depends on cell-wall assembly. *Proc Natl Acad Sci U S A* **108**, 15822-15827 (2011).
60. B. P. Bratton, J. W. Shaevitz, Z. Gitai, R. M. Morgenstein, MreB polymers and curvature localization are enhanced by RodZ and predict E. coli's cylindrical uniformity. *Nat Commun* **9**, 2797 (2018).
61. S. Hussain *et al.*, MreB filaments align along greatest principal membrane curvature to orient cell wall synthesis. *Elife* **7**, e32471 (2018).
62. R. M. Morgenstein *et al.*, RodZ links MreB to cell wall synthesis to mediate MreB rotation and robust morphogenesis. *Proc Natl Acad Sci U S A* **112**, 12510-12515 (2015).
63. R. Ago, D. Shiomi, RodZ: a key-player in cell elongation and cell division in Escherichia coli. *AIMS Microbiol* **5**, 358-367 (2019).
64. F. O. Bendezu, C. A. Hale, T. G. Bernhardt, P. A. de Boer, RodZ (YfgA) is required for proper assembly of the MreB actin cytoskeleton and cell shape in E. coli. *EMBO J* **28**, 193-204 (2009).

880 65. F. van den Ent, C. M. Johnson, L. Persons, P. de Boer, J. Lowe, Bacterial actin
881 MreB assembles in complex with cell shape protein RodZ. *EMBO J* **29**, 1081-1090
882 (2010).
883 66. A. J. Meeske *et al.*, SEDS proteins are a widespread family of bacterial cell wall
884 polymerases. *Nature* **537**, 634-638 (2016).
885 67. P. D. A. Rohs *et al.*, A central role for PBP2 in the activation of peptidoglycan
886 polymerization by the bacterial cell elongation machinery. *PLoS Genet* **14**,
887 e1007726 (2018).
888 68. P. D. A. Rohs *et al.*, Identification of potential regulatory domains within the MreC
889 and MreD components of the cell elongation machinery. *J Bacteriol*
890 10.1128/JB.00493-20 (2021).
891 69. M. Sjodt *et al.*, Structure of the peptidoglycan polymerase RodA resolved by
892 evolutionary coupling analysis. *Nature* **556**, 118-121 (2018).
893 70. M. Sjodt *et al.*, Structural coordination of polymerization and crosslinking by a
894 SEDS-bPBP peptidoglycan synthase complex. *Nat Microbiol* **5**, 813-820 (2020).
895 71. H. Cho *et al.*, Bacterial cell wall biogenesis is mediated by SEDS and PBP
896 polymerase families functioning semi-autonomously. *Nat Microbiol* **1**, 16172
897 (2016).
898 72. M. F. Dion *et al.*, Bacillus subtilis cell diameter is determined by the opposing
899 actions of two distinct cell wall synthetic systems. *Nat Microbiol* **4**, 1294-1305
900 (2019).
901 73. M. Pazos, W. Vollmer, Regulation and function of class A Penicillin-binding
902 proteins. *Curr Opin Microbiol* **60**, 80-87 (2021).
903 74. A. Vigouroux *et al.*, Class-A penicillin binding proteins do not contribute to cell
904 shape but repair cell-wall defects. *Elife* **9**, e51998 (2020).
905 75. K. H. Berg, G. A. Stamsas, D. Straume, L. S. Havarstein, Effects of low PBP2b
906 levels on cell morphology and peptidoglycan composition in Streptococcus
907 pneumoniae R6. *J Bacteriol* **195**, 4342-4354 (2013).
908 76. J. Philippe, T. Vernet, A. Zapun, The elongation of ovococci. *Microb Drug Resist*
909 **20**, 215-221 (2014).
910 77. G. A. Stamsas *et al.*, Identification of EloR (Spr1851) as a regulator of cell
911 elongation in Streptococcus pneumoniae. *Mol Microbiol* **105**, 954-967 (2017).
912 78. D. Straume, G. A. Stamsas, K. H. Berg, Z. Salehian, L. S. Havarstein, Identification
913 of pneumococcal proteins that are functionally linked to penicillin-binding protein
914 2b (PBP2b). *Mol Microbiol* **103**, 99-116 (2017).
915 79. J. J. Zheng, A. J. Perez, H. T. Tsui, O. Massidda, M. E. Winkler, Absence of the
916 KhpA and KhpB (JAG/EloR) RNA-binding proteins suppresses the requirement for
917 PBP2b by overproduction of FtsA in Streptococcus pneumoniae D39. *Mol*
918 *Microbiol* **106**, 793-814 (2017).
919 80. H. C. Tsui *et al.*, Suppression of a deletion mutation in the gene encoding essential
920 PBP2b reveals a new lytic transglycosylase involved in peripheral peptidoglycan
921 synthesis in Streptococcus pneumoniae D39. *Mol Microbiol* **100**, 1039-1065
922 (2016).
923 81. A. D. Land, M. E. Winkler, The requirement for pneumococcal MreC and MreD is
924 relieved by inactivation of the gene encoding PBP1a. *J Bacteriol* **193**, 4166-4179
925 (2011).

926 82. A. Taguchi, J. E. Page, H. T. Tsui, M. E. Winkler, S. Walker, Biochemical
927 reconstitution defines new functions for membrane-bound glycosidases in
928 assembly of the bacterial cell wall. *Proc Natl Acad Sci U S A* **118** (2021).
929 83. A. K. Fenton, L. El Mortaji, D. T. Lau, D. Z. Rudner, T. G. Bernhardt, CozE is a
930 member of the MreCD complex that directs cell elongation in Streptococcus
931 pneumoniae. *Nat Microbiol* **2**, 16237 (2016).
932 84. M. M. Lamanna, A. T. Maurelli, What Is Motion? Recent Advances in the Study of
933 Molecular Movement Patterns of the Peptidoglycan Synthesis Machines. *J*
934 *Bacteriol* **204**, e0059821 (2022).
935 85. C. Lenoir *et al.*, The morphogenic protein CopD controls the spatio-temporal
936 dynamics of PBP1a and PBP2b in Streptococcus pneumoniae. *mBio* **14**,
937 e0141123 (2023).
938 86. S. G. Bartual *et al.*, Structural basis of PcsB-mediated cell separation in
939 Streptococcus pneumoniae. *Nature communications* **5**, 3842 (2014).
940 87. B. E. Rued *et al.*, Structure of the Large Extracellular Loop of FtsX and Its
941 Interaction with the Essential Peptidoglycan Hydrolase PcsB in Streptococcus
942 pneumoniae. *mBio* **10** (2019).
943 88. L. T. Sham, S. M. Barendt, K. E. Kopecky, M. E. Winkler, Essential PcsB putative
944 peptidoglycan hydrolase interacts with the essential FtsXSpn cell division protein
945 in Streptococcus pneumoniae D39. *Proc Natl Acad Sci U S A* **108**, E1061-1069
946 (2011).
947 89. L. T. Sham, K. R. Jensen, K. E. Bruce, M. E. Winkler, Involvement of FtsE ATPase
948 and FtsX extracellular loops 1 and 2 in FtsEX-PcsB complex function in cell
949 division of Streptococcus pneumoniae D39. *mBio* **4** (2013).
950 90. P. Domínguez-Cuevas, I. Porcelli, R. A. Daniel, J. Errington, Differentiated roles
951 for MreB-actin isologues and autolytic enzymes in Bacillus subtilis morphogenesis.
952 *Mol Microbiol* **89**, 1084-1098 (2013).
953 91. J. Meisner *et al.*, FtsEX is required for CwlO peptidoglycan hydrolase activity
954 during cell wall elongation in Bacillus subtilis. *Mol Microbiol* **89**, 1069-1083 (2013).
955 92. M. J. Catalão, J. Figueiredo, M. X. Henriques, J. P. Gomes, S. R. Filipe,
956 Optimization of fluorescent tools for cell biology studies in Gram-positive bacteria.
957 *PLoS One* **9**, e113796 (2014).
958 93. J. B. Grimm *et al.*, A general method to improve fluorophores for live-cell and
959 single-molecule microscopy. *Nat Methods* **12**, 244-250, 243 p following 250
960 (2015).
961 94. M. X. Henriques, M. J. Catalão, J. Figueiredo, J. P. Gomes, S. R. Filipe,
962 Construction of improved tools for protein localization studies in Streptococcus
963 pneumoniae. *PLoS One* **8**, e55049 (2013).
964 95. G. V. Los *et al.*, HaloTag: a novel protein labeling technology for cell imaging and
965 protein analysis. *ACS Chem Biol* **3**, 373-382 (2008).
966 96. K. Peters *et al.*, Streptococcus pneumoniae PBP2x mid-cell localization requires
967 the C-terminal PASTA domains and is essential for cell shape maintenance. *Mol*
968 *Microbiol* **92**, 733-755 (2014).
969 97. N. Ke, D. Landgraf, J. Paulsson, M. Berkmen, Visualization of Periplasmic and
970 Cytoplasmic Proteins with a Self-Labeling Protein Tag. *J Bacteriol* **198**, 1035-1043
971 (2016).

98. A. Eberhardt, L. J. Wu, J. Errington, W. Vollmer, J. W. Veening, Cellular localization of choline-utilization proteins in Streptococcus pneumoniae using novel fluorescent reporter systems. *Mol Microbiol* **74**, 395-408 (2009).
99. F. E. Jacobsen, K. M. Kazmierczak, J. P. Lisher, M. E. Winkler, D. P. Giedroc, Interplay between manganese and zinc homeostasis in the human pathogen Streptococcus pneumoniae. *Metallomics : integrated biometal science* **3**, 38-41 (2011).
100. J. W. McCausland *et al.*, Treadmilling FtsZ polymers drive the directional movement of sPG-synthesis enzymes via a Brownian ratchet mechanism. *Nat Commun* **12**, 609 (2021).
101. H. T. Tsui *et al.*, Negative regulation of MurZ and MurA underlies the essentiality of GpsB- and StkP-mediated protein phosphorylation in Streptococcus pneumoniae D39. *Mol Microbiol* **120**, 351-383 (2023).
102. O. Kocaoglu, H. C. Tsui, M. E. Winkler, E. E. Carlson, Profiling of β-lactam selectivity for penicillin-binding proteins in Streptococcus pneumoniae D39. *Antimicrob Agents Chemother* **59**, 3548-3555 (2015).
103. K. H. Berg, D. Straume, L. S. Havarstein, The function of the transmembrane and cytoplasmic domains of pneumococcal penicillin-binding proteins 2x and 2b extends beyond that of simple anchoring devices. *Microbiology (Reading)* **160**, 1585-1598 (2014).
104. H. Cho, T. Uehara, T. G. Bernhardt, Beta-lactam antibiotics induce a lethal malfunctioning of the bacterial cell wall synthesis machinery. *Cell* **159**, 1300-1311 (2014).
105. I. Shlosman *et al.*, Allosteric activation of cell wall synthesis during bacterial growth. *Nat Commun* **14**, 3439 (2023).
106. N. Tarantino *et al.*, TNF and IL-1 exhibit distinct ubiquitin requirements for inducing NEMO-IKK supramolecular structures. *J Cell Biol* **204**, 231-245 (2014).
107. J. Y. Tinevez *et al.*, TrackMate: An open and extensible platform for single-particle tracking. *Methods* **115**, 80-90 (2017).
108. T. K. Lee *et al.*, A dynamically assembled cell wall synthesis machinery buffers cell growth. *Proc Natl Acad Sci U S A* **111**, 4554-4559 (2014).
109. G. Ozbaykal *et al.*, The transpeptidase PBP2 governs initial localization and activity of the major cell-wall synthesis machinery in E. coli. *Elife* **9** (2020).
110. C. H. Bohrer, J. Xiao, Complex Diffusion in Bacteria. *Adv Exp Med Biol* **1267**, 15-43 (2020).
111. A. Kusumi, Y. Sako, M. Yamamoto, Confined lateral diffusion of membrane receptors as studied by single particle tracking (nanovid microscopy). Effects of calcium-induced differentiation in cultured epithelial cells. *Biophys J* **65**, 2021-2040 (1993).
112. L. Pasquina-Lemonche *et al.*, The architecture of the Gram-positive bacterial cell wall. *Nature* **582**, 294-297 (2020).
113. S. Middlemiss *et al.*, Molecular motor tug-of-war regulates elongasome cell wall synthesis dynamics in Bacillus subtilis. *bioRxiv* 10.1101/2023.05.10.540107, 2023.2005.2010.540107 (2023).

114. Z. Lyu *et al.*, FtsN maintains active septal cell wall synthesis by forming a processive complex with the septum-specific peptidoglycan synthases in E. coli. *Nat Commun* **13**, 5751 (2022).
115. D. Straume *et al.*, Class A PBPs have a distinct and unique role in the construction of the pneumococcal cell wall. *Proc Natl Acad Sci U S A* **117**, 6129-6138 (2020).
116. W. M. Figueroa-Cuilan, P. J. B. Brown, Cell Wall Biogenesis During Elongation and Division in the Plant Pathogen Agrobacterium tumefaciens. *Curr Top Microbiol Immunol* **418**, 87-110 (2018).
117. M. A. Williams *et al.*, Unipolar Peptidoglycan Synthesis in the Rhizobiales Requires an Essential Class A Penicillin-Binding Protein. *mBio* **12**, e0234621 (2021).
118. A. R. Winther, M. Kjos, M. L. Herigstad, L. S. Havarstein, D. Straume, EloR interacts with the lytic transglycosylase MltG at midcell in Streptococcus pneumoniae R6. *J Bacteriol* 10.1128/JB.00691-20 (2021).

FIGURE LEGENDS

Fig. 1. Elongation PG synthesis proteins display processive circumferential motion, and a limited number of molecules engage in PG synthesis simultaneously. Sm-TIRFm was performed at 1 FPS as described in *Materials and Methods* on strains *iht-pbp2b* (IU15928), *iht-pbp2b* // P_{Zn}-*iht-pbp2b* (IU16553), *iht-rodA* (IU15970), *iht-rodA* // P_{Zn}-*iht-rodA* (IU16496), *iht-mreC* (IU16344), *iht-pbp1a* (IU16320), *iht-pbp1a* // P_{Zn}-*iht-pbp1a* (IU16497) and *iht-mpgA* (IU15997). (*A*) Representative time-lapse images and kymographs of molecules displaying processive circumferential movement in strains IU15928, IU15970, IU16344 and IU16497. Cell outlines are green (DICm) and HT-labeled molecules are magenta. Location of lines used to make kymographs are shown in the time lapse images (yellow dashed lines). For each protein, the left kymograph was generated from the cell depicted in the time-lapse images. Numbers (1-3) denote when each image in the time lapse was taken. The other two kymographs are from cells that are not shown. Calculation of circumferential velocities from kymographs are described in *Materials and Methods*. Scale bars are 1 µm. (*B*) Movement patterns of HT-labeled molecules. Bars represent the mean relative frequency of each type of motion. For a given

1046 strain or condition, the relative frequencies of circumferential, diffusive, and static
1047 molecules were determined for each biological replicate. Frequencies were then
1048 averaged over all replicates to determine the mean (error bars represent ± SD). Mean
1049 values are annotated above each bar, and the total number of molecules analyzed (n)
1050 from the number of biological replicates (R) for each strain is below each strain or
1051 condition. Circumferential (red), diffusive (blue), and static (grey) movement patterns are
1052 shown. Circumferentially moving molecules were defined as molecules moving in one
1053 direction for 6 or more frames (at 1 FPS imaging rate) with a linear velocity ≥ 5 nm/s.
1054 Static molecules were defined as molecules not moving or moving for 6 or more frames
1055 with a velocity < 5 nm/s. Diffusive molecules were defined as molecules that moved, but
1056 not in a consistent direction, for 6 or more non-consecutive frames within a period of 90
1057 s. Full criteria for determining movement patterns are described in *Materials and Methods*.
1058 The expression level of iHT-fusion proteins relative to the untagged WT level is shown as
1059 a percentage under the strain names. iHT-fusion proteins are expressed solely from the
1060 native chromosomal locus or with an additional copy of the gene encoding the iHT-fusion
1061 protein at an ectopic site under control of a zinc-inducible promoter, with 0 or 0.25 mM Zn
1062 inducer added. Unpaired t-tests were performed to compare relative frequencies of
1063 motion types. *ns* (nonsignificant); *$P < 0.05$; **$P < 0.01$; ***$P < 0.001$; ****$P < 0.0001$.

1064 **Fig. 2.** Diffusively moving components of the core PG elongasome do not actively
1065 synthesize PG (blue) in non-midcell regions of exponentially growing pneumococcal cells.
1066 3D-SIM images, where iHT-bPBP2b is red, regions of PBP transpeptidase activity is blue,
1067 and midcell regions include septa of dividing cells and equators of predivisional daughter
1068 cells. Cells were grown in BHI ± 0.3 mM Zn inducer, labeled with a saturating amount of

1069 HT-ligand for 15 min, washed, labeled with 400 μM of the fluorescent D-amino acid HADA
1070 (blue) for 2.5 min, fixed, and imaged as described in *Materials and Methods*. Images are
1071 summed from 15 *Z* plane sections (*Z*-stack) representing a total depth of 1.875 μm.
1072 Percentages indicate the amount of iHT-bPBP2b expressed relative to the untagged WT
1073 bPBP2b^{+} level (32). (*A*) *iht-pbp2b* (IU15928) and (*B*) *iht-pbp2b* // P_{Zn}-*iht-pbp2b* (IU16553).
1074 Scale bar is 1 μm.

1075 **Fig. 3.** bPBP2b, RodA, and MreC form a stable complex during active PG synthesis.
1076 Dot plots of (*A*) circumferential velocities and (*B*) circumferential durations of elongation
1077 PG synthesis proteins determined by sm-TIRFm at 1 FPS. Strains are the same as in Fig.
1078 1. +Zn condition indicates 0.25 mM Zn inducer was added. Black and red lines are median
1079 ± interquartile, and mean ± SD are indicated. n = total molecules analyzed from 2-5
1080 biological replicates. Dotted grey lines indicate the minimum thresholds for (*A*) velocity (5
1081 nm/s) and (*B*) duration (6 s). A Kruskal-Wallis with Dunn's multiple comparisons test was
1082 used to compare circumferential velocities or circumferential durations in different strains.
1083 *ns* (nonsignificant); $^{**}P < 0.01$; $^{***}P < 0.001$; $^{****}P < 0.0001$.

1084 **Fig. 4.** Circumferential movement of bPBP2b and RodA is independent of FtsZ
1085 treadmilling and reflective of PG synthesis. Sm-TIRFm was performed at 1 FPS on strains
1086 expressing iHT-bPBP2b or iHT-RodA. Dot plots of circumferential velocities are shown.
1087 Black and red lines are median ± interquartile, and mean ± SD are indicated. (*A*) Both *iht-*
1088 *pbp2b* (black, IU15928) and *iht-pbp2b* P_{Zn}-*ftsZ*(D214A) (red, IU16091) strains were
1089 supplemented with 0.25 mM Zn inducer. (*B*) IU16056 expresses both iHT-bPBP2b and
1090 FtsZ-sfGFP. The treadmilling velocity of FtsZ-sfGFP filaments (green) and the
1091 circumferential velocity of iHT-bPBP2b single molecules (red) were determined. (*C*) *iht-*

1092 *pbp2b* (black, IU15928) and *iht-pbp2b* Δ*murZ* (red, IU16110) strains. (*D*) *iht-rodA* (black,
1093 IU15970) and *iht-rodA* Δ*murZ* (blue, IU16112) strains. n = total molecules analyzed from
1094 2 biological replicates. Circumferential velocities in different strains were compared using
1095 a Mann-Whitney test. *$P < 0.05$; ****$P < 0.0001$.

1096 **Fig. 5.** The catalytic activities of bPBP2b and RodA are required for cell viability and
1097 PG synthesis, but not localization. (*A*) Diagram of merodiploid strains containing catalytic
1098 mutant alleles fused to the HaloTag at the native locus and the Zn-inducible WT allele at
1099 the ectopic site. (*B*) Representative growth curves of WT (black square, IU1824), *iht-*
1100 *pbp2b* (red square, IU15928), *iht-rodA* (blue square, IU15970), Δ*pbp2b* // P_{Zn}-*pbp2b*
1101 (green, IU11258), *iht-pbp2b*(S391A) // P_{Zn}-*pbp2b* (red, IU16232), and *iht-rodA*(D283A) //
1102 P_{Zn}-*rodA* (blue, IU16239) strains grown in C+Y medium with or without 0.2 mM Zn inducer
1103 as described in the section on ectopic expression and depletion conditions in *Materials*
1104 *and Methods*. The experiment was repeated twice with similar results. (*C* and *D*) sm-
1105 TIRFm was performed at 1 FPS on strains IU16232 and IU16239. (*C*) Movement patterns
1106 of iHT-bPBP2b(S391A) (IU16232) and iHT-RodA(D283A) (IU16239). The layout is the
1107 same as Fig. 1*B* (see legend for details). Unpaired t-tests were performed to compare
1108 relative frequencies of motion types. *ns* (nonsignificant); **$P < 0.01$; ***$P < 0.001$; ****$P <$
1109 0.0001. (*D*) Representative montages and kymographs of static molecules from strains
1110 IU16232 and IU16239 (without Zn inducer for 3 h) are displayed as described for Fig. 1*A*,
1111 except the scale bar is 0.5 μm. (*E*) 2D-FM of catalytically inactive proteins. Strains
1112 IU16232 and IU16239 were grown without Zn (see Fig. 5*B*) and labeled with saturating
1113 amounts of HT-ligand. HT-fusion proteins are shown in magenta. Scale bar is 1 μm. The
1114 experiment was repeated twice with similar results.

1115 **Fig. 6.** bPBP2b localization becomes diffuse and circumferential movement is lost
1116 upon MreC depletion. (*A*) 2D-FM of strains *iht-pbp2b* (left, IU15928) and *iht-pbp2b* Δ*mreC*
1117 // P_{Zn}-*mreC* (right, IU16281). Cells were grown in C+Y media with or without (depletion)
1118 0.2 mM Zn inducer, labeled with saturating amounts of HT-ligand, and imaged after 3 h.
1119 See the section on ectopic expression and depletion conditions in *Materials and Methods*
1120 for details. The experiment was repeated twice with similar results. (*B*) sm-TIRFm was
1121 performed at 1 FPS on strains *iht-pbp2b* (IU15928) and *iht-pbp2b* Δ*mreC* // P_{Zn}-*mreC*
1122 (IU16281) after 3 h of growth in C+Y media without Zn inducer (depletion). The layout is
1123 the same as Fig. 1*B* (see legend for details). Unpaired t-tests were performed to compare
1124 relative frequencies of motion types. *ns* (nonsignificant); $*P < 0.05$; $**P < 0.01$.

1125 **Fig. 7.** bPBP2b and RodA require each other for localization and motion. 2D-FM and
1126 sm-TIRFm at 1 FPS were performed on strains *iht-pbp2b* Δ*rodA* // P_{Zn}-*rodA* (IU16204)
1127 and *iht-rodA* Δ*pbp2b* // P_{Zn}-*pbp2b* (IU16202). (*A* and *B*) 2D-FM showing localization in
1128 cells of strains (*A*) iHT-bPBP2b (IU16204) and (*B*) iHT-RodA (IU16202) grown with or
1129 without (depletion; depl.) 0.2 mM Zn inducer for 3 h and labeled with saturating amounts
1130 of HT-ligand. See the section on ectopic expression and depletion conditions in *Materials*
1131 *and Methods* for additional details. The experiment was repeated twice with similar
1132 results. (*C* to *E*) sm-TIRFm was performed at 1 FPS on IU16204 and IU16202 without Zn
1133 inducer (depletion) for 3 hours. (*C*) Movement patterns of HT-labeled molecules. Results
1134 for the *iht-pbp2b* Δ*rodA* // P_{Zn}-*rodA* (IU16204) and *iht-rodA* Δ*pbp2b* // P_{Zn}-*pbp2b* (IU16202)
1135 strains were determined and are graphed with data for *iht-pbp2b* (IU15928) and *iht-rodA*
1136 (IU15970) replotted from Fig. 1*B* for comparison. The layout is the same as Fig. 1*B* (see
1137 legend for details). Unpaired t-tests were performed to compare relative frequencies of

1138 motion types. *ns* (nonsignificant), *$P < 0.05$; **$P < 0.01$; ***$P < 0.001$. (*D* and *E*) Dot plots
1139 of circumferential velocities with mean values ± SD indicated for (*D*) strains IU15928
1140 (black) and IU16204 (red), and (*E*) strains IU15970 (black) and IU16202 (red). Data from
1141 stains IU15928 and IU15970 are replotted from Fig. 3*A* for comparison. Black and red
1142 lines are median ± interquartile, and mean ± SD are indicated. n = total molecules
1143 analyzed from 2 biological replicates. A Mann-Whitney test was used to compare
1144 velocities upon protein depletion (depl.). *ns* (nonsignificant).

1145 **Fig. 8.** Circumferential movement of aPBP1a reflects active PG synthesis. Sm-TIRFm
1146 was performed at 1 FPS as described in *Materials and Methods* on strains *iht-pbp1a* //
1147 P_{Zn}-*iht-pbp1a* (IU16497) and *iht-pbp1a*(S370A) // P_{Zn}-*iht-pbp1a*(S370A) (IU19168) with
1148 0.25 mM Zn added. Movement patterns of HT-labeled molecules at sites of PG synthesis
1149 (midcell) or elsewhere in the cell (non-midcell) were analyzed. The layout is the same as
1150 Fig. 1*B* (see legend for details). A two-way ANOVA with Tukey's multiple comparison test
1151 was used to compare relative frequencies of motion types among strains. *$P < 0.05$.

1152 **Fig. 9.** MpgA displays confined subdiffusive movement at midcell. Sm-TIRFm was
1153 performed on strains *iht-mpgA* (IU15997) and *iht-mreC* (IU16344). Representative
1154 kymographs of (*A*) iHT-MpgA molecules moving at sites of PG synthesis imaged at 1 FPS
1155 and (*B*) iHT-MpgA and iHT-MreC molecules imaged at 10 FPS. (*C*) Dot plots of velocities
1156 determined at 10 FPS over short runs of iHT-MpgA molecules in midcell regions (black)
1157 and at non-midcell regions (red). Black and red lines are median ± interquartile, and mean
1158 ± SD are indicated. n = total molecules analyzed from 2 biological replicates. Velocities
1159 in different regions of cells were compared using a Mann-Whitney test. ****$P < 0.0001$.

1160 **Fig. 10.** Components of the pneumococcal core PG elongasome and proteins
1161 implicated in elongation PG synthesis exhibit different patterns of confined diffusion. Sm-
1162 TIRFm was performed at 20 FPS on strains *iht-pbp2b* // P_{Zn}-*iht-pbp2b* (IU16553), *iht-rodA*
1163 // P_{Zn}-*iht-rodA* (IU16496), *iht-mreC* (IU16344), *iht-pbp1a* // P_{Zn}-*iht-pbp1a* (IU16497) and
1164 *iht-mpgA* (IU15997). 0.25 mM Zn inducer was added to strains IU16553, IU16496 and
1165 IU16497. (*A*) Representative fields of cells containing multiple single-molecule
1166 trajectories (colored lines) classified as diffusive (top row) and non-diffusive (bottom row).
1167 Trajectories with a displacement > 0.13 μm and a velocity standard deviation > 0.63 μm/s
1168 were defined as diffusive, and the remaining trajectories were defined as non-diffusive.
1169 Full details of trajectory constructions and classification criteria are described in *Materials*
1170 *and Methods*. The color of each trajectory line segment represents the displacement (in
1171 nm) of the molecule from one frame to the next. Scale bar is 1 μm. (*B*) Mean square
1172 displacements (MSD) were calculated for diffusive and non-diffusive trajectories. Circles
1173 show MSD values, and error bars represent SEM. Lines represent MSD curves fit to the
1174 data as described in *Materials and Methods*. To the right of the graph are the mean
1175 diffusion coefficients (± SEM) of diffusive trajectories, alpha values of diffusive trajectories
1176 (α), the percent of total trajectories that were classified as diffusive (% diffusive), and the
1177 total number of trajectories (n) analyzed from 2 biological replicates. α values < 1 indicate
1178 that molecules are exhibiting confined diffusion (or subdiffusion), discussed in the text.
1179 The diffusion coefficients were compared between strains using a Brown-Forsythe and
1180 Welch's ANOVA with a Games-Howell multiple comparisons test. $^{**}P < 0.01$.

1181 **Fig. 11.** Summary model of (*A*) the composition and dynamics of core elongasome
1182 components (bPBP2b, RodA, and MreC) and proteins linked to PG elongation synthesis

1183 (aPBP1a and MpgA) in growing *S. pneumoniae* cells; and (*B*) the distribution of these
1184 proteins when underexpressed (left) or expressed at WT levels (right). (*A*) The
1185 circumferential, processive movement of bPBP2b, RodA, and MreC reported here likely
1186 apply to the other core elongasome components RodZ and MreD. In early, predivisional
1187 cells, the core PG elongasome is located in the FtsZ-ring at the equator midcell of a
1188 daughter cell. In later divisional cells, the core PG elongasome is in the outer ring of the
1189 midcell septal annular disk. The motion of MreC is the same in early or late divisional
1190 cells. Class A aPBP1a also displays circumferential, processive motion at midcell that
1191 depends on PG synthesis, but its dynamics indicate that aPBP1a is not a persistent
1192 member of the core PG elongasome, although short interactions are possible. In contrast,
1193 MpgA moves in a distinctive type of subdiffusion that is largely confined to the midcell
1194 region. Components of the core elongasome and aPBP1a move diffusively outside of
1195 midcell rings. There are also nonmoving, static molecules (> 6 s) of elongasome proteins
1196 and aPBP1a, mainly in midcell regions. It is not clear whether static molecules are
1197 synthesizing PG or are in a non-synthesizing transition state. In addition, diffusing
1198 molecules of aPBP1a and MpgA were infrequently detected pausing (< 1s) before
1199 resuming motion. See text for additional information. (*B*) When underexpressed,
1200 components of the core PG elongasome are largely confined to PG synthesis at midcell
1201 septa and the equators of predivisional daughter cells starting to divide. In contrast, when
1202 expressed at WT levels, most components of the PG elongasome (and aPBP1a) are
1203 diffusing over the cell surface and are not synthesizing PG. Thus, elongasome
1204 components and aPBP1a are in excess in growing cells, and only a limited number
1205 engage in midcell PG synthesis. In contrast, subdiffusion of MpgA molecules expressed

1206 at the WT level is largely confined to the midcell region by an unknown mechanism. See

1207 text for additional details.

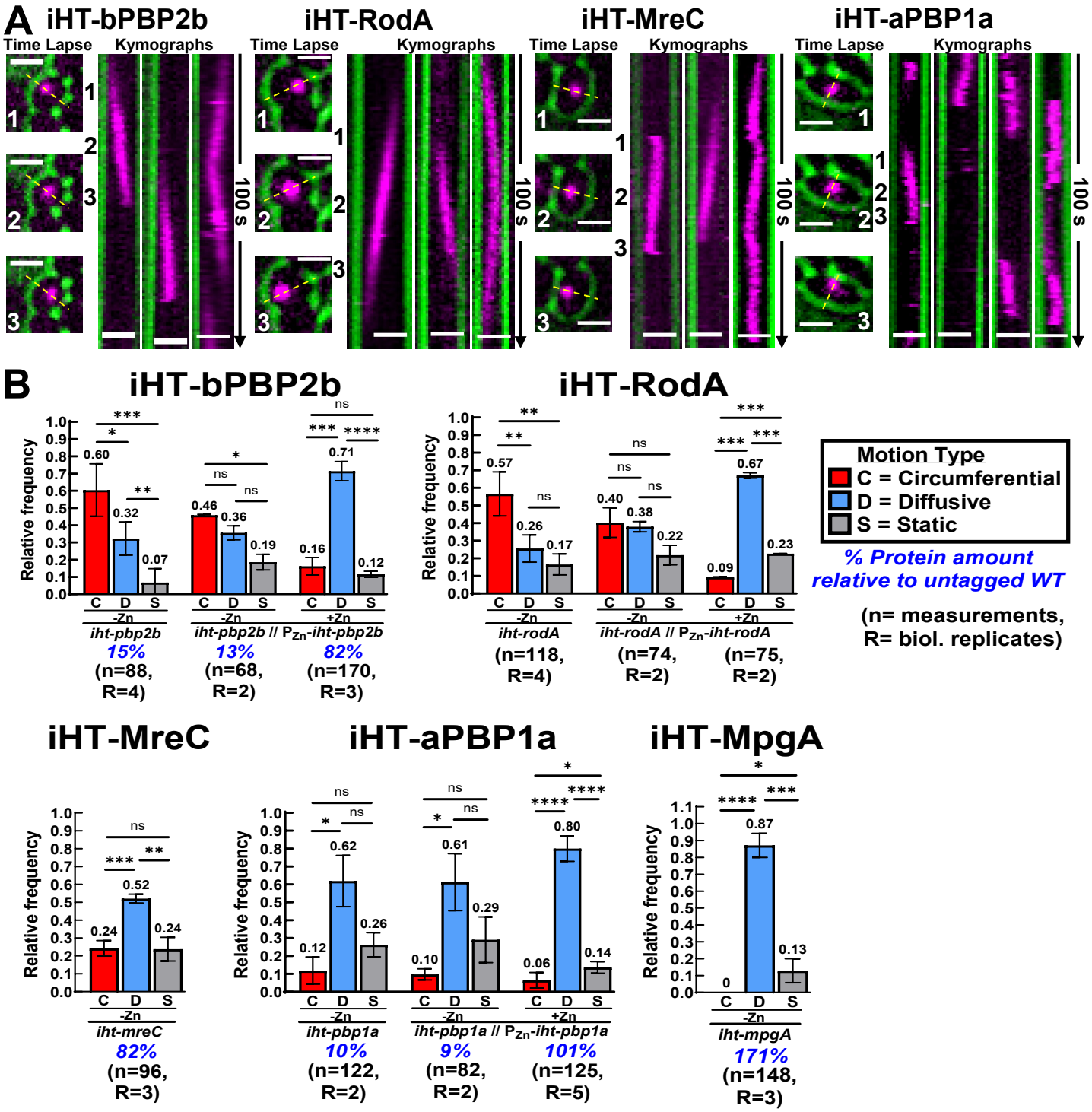
A
iHT-bPBP2b
iHT-RodA
iHT-MreC
iHT-aPBP1a
Time Lapse
Kymographs
100 s
B
iHT-bPBP2b
Relative frequency
0.60
0.32
0.07
0.46
0.36
0.19
0.16
0.71
0.12
C D S
-Zn
+Zn
iht-pbp2b
iht-pbp2b // PZn-iht-pbp2b
15%
(n=88, R=4)
13%
(n=68, R=2)
82%
(n=170, R=3)
iHT-RodA
0.57
0.26
0.17
0.40
0.38
0.22
0.09
0.67
0.23
iht-rodA
iht-rodA // PZn-iht-rodA
(n=118, R=4)
(n=74, R=2)
(n=75, R=2)
Motion Type
C = Circumferential
D = Diffusive
S = Static
% Protein amount relative to untagged WT
(n= measurements, R= biol. replicates)
iHT-MreC
0.24
0.52
0.24
iht-mreC
82%
(n=96, R=3)
iHT-aPBP1a
0.12
0.62
0.26
0.10
0.61
0.29
0.06
0.80
0.14
iht-pbp1a
iht-pbp1a // PZn-iht-pbp1a
10%
(n=122, R=2)
9%
(n=82, R=2)
101%
(n=125, R=5)
iHT-MpgA
0
0.87
0.13
iht-mpgA
171%
(n=148, R=3)

Fig. 1.

Fig. 1. Elongation PG synthesis proteins display processive circumferential motion, and a limited number of molecules engage in PG synthesis simultaneously. Sm-TIRFm was performed at 1 FPS as described in *Materials and Methods* on strains *iht-pbp2b* (IU15928), *iht-pbp2b* // P_{Zn}-*iht-pbp2b* (IU16553), *iht-rodA* (IU15970), *iht-rodA* // P_{Zn}-*iht-rodA* (IU16496), *iht-mreC* (IU16344), *iht-pbp1a* (IU16320), *iht-pbp1a* // P_{Zn}-*iht-pbp1a* (IU16497) and *iht-mpgA* (IU15997). (*A*) Representative time-lapse images and kymographs of molecules displaying processive circumferential movement in strains IU15928, IU15970, IU16344 and IU16497. Cell outlines are green (DICm) and HT-labeled molecules are magenta. Location of lines used to make kymographs are shown in the time lapse images (yellow dashed lines). For each protein, the left kymograph was generated from the cell depicted in the time-lapse images. Numbers (1-3) denote when each image in the time lapse was taken. The other two kymographs are from cells that are not shown. Calculation of circumferential velocities from kymographs are described in *Materials and Methods*. Scale bars are 1 μm. (*B*) Movement patterns of HT-labeled molecules. Bars represent the mean relative frequency of each type of motion. For a given strain or condition, the relative frequencies of circumferential, diffusive, and static molecules were determined for each biological replicate. Frequencies were then averaged over all replicates to determine the mean (error bars represent ± SD). Mean values are annotated above each bar, and the total number of molecules analyzed (n) from the number of biological replicates (R) for each strain is below each strain or condition. Circumferential (red), diffusive (blue), and static (grey) movement patterns are shown. Circumferentially moving molecules were defined as molecules moving in one direction for 6 or more frames (at 1 FPS imaging rate) with a linear velocity ≥ 5 nm/s. Static molecules were defined as molecules not moving or moving for 6 or more frames with a velocity < 5 nm/s. Diffusive molecules were defined as molecules that moved, but not in a consistent direction, for 6 or more non-consecutive frames within a period of 90 s. Full criteria for determining movement patterns are described in *Materials and Methods*. The expression level of iHT-fusion proteins relative to the untagged WT level is shown as a percentage under the strain names. iHT-fusion proteins are expressed solely from the native chromosomal locus or with an additional copy of the gene encoding the iHT-fusion protein at an ectopic site under control of a zinc-inducible promoter, with 0 or 0.25 mM Zn inducer added. Unpaired t-tests were performed to compare relative frequencies of motion types. *ns* (nonsignificant); **P* < 0.05; ***P* < 0.01; ****P* < 0.001; *****P* < 0.0001.

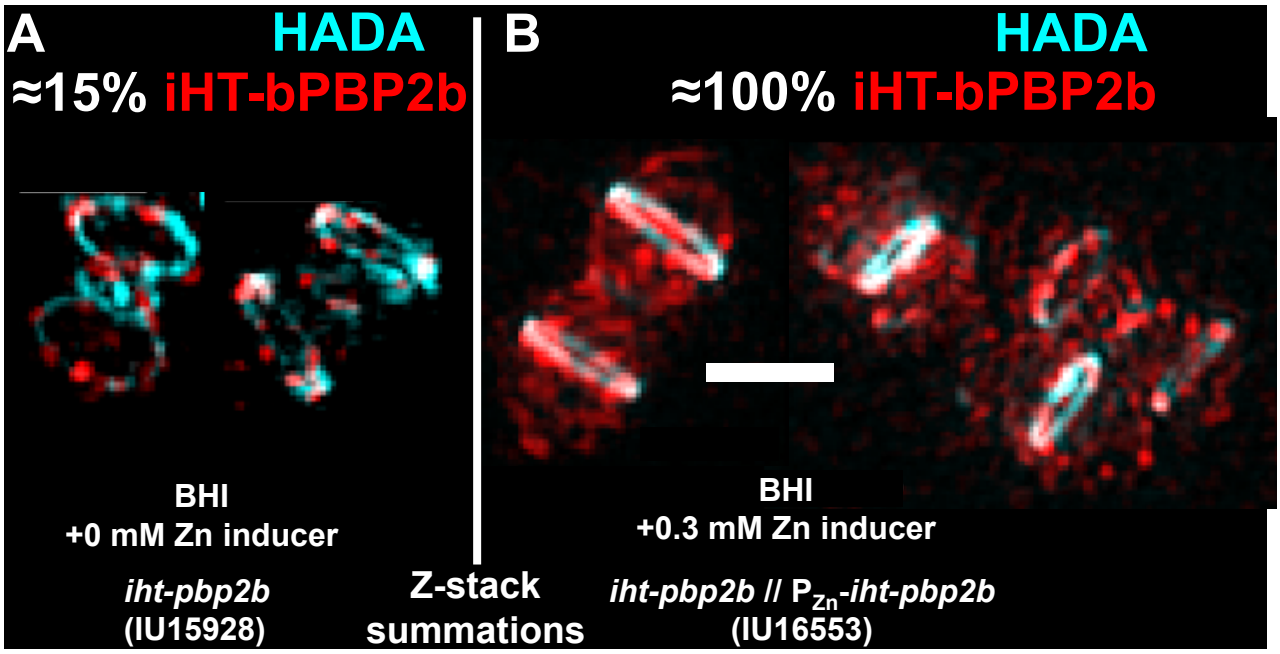

Fig. 2. Diffusively moving components of the core PG elongasome do not actively synthesize PG (blue) in non-midcell regions of exponentially growing pneumococcal cells. 3D-SIM images, where iHT-bPBP2b is red, regions of PBP transpeptidase activity is blue, and midcell regions include septa of dividing cells and equators of predivisional daughter cells. Cells were grown in BHI ± 0.3 mM Zn inducer, labeled with a saturating amount of HT-ligand for 15 min, washed, labeled with 400 μM of the fluorescent D-amino acid HADA (blue) for 2.5 min, fixed, and imaged as described in *Materials and Methods*. Images are summed from 15 *Z* plane sections (*Z*-stack) representing a total depth of 1.875 μm. Percentages indicate the amount of iHT-bPBP2b expressed relative to the untagged WT bPBP2b^{+} level (32). (*A*) *iht-pbp2b* (IU15928) and (*B*) *iht-pbp2b* // P_{Zn}-*iht-pbp2b* (IU16553). Scale bar is 1 μm.

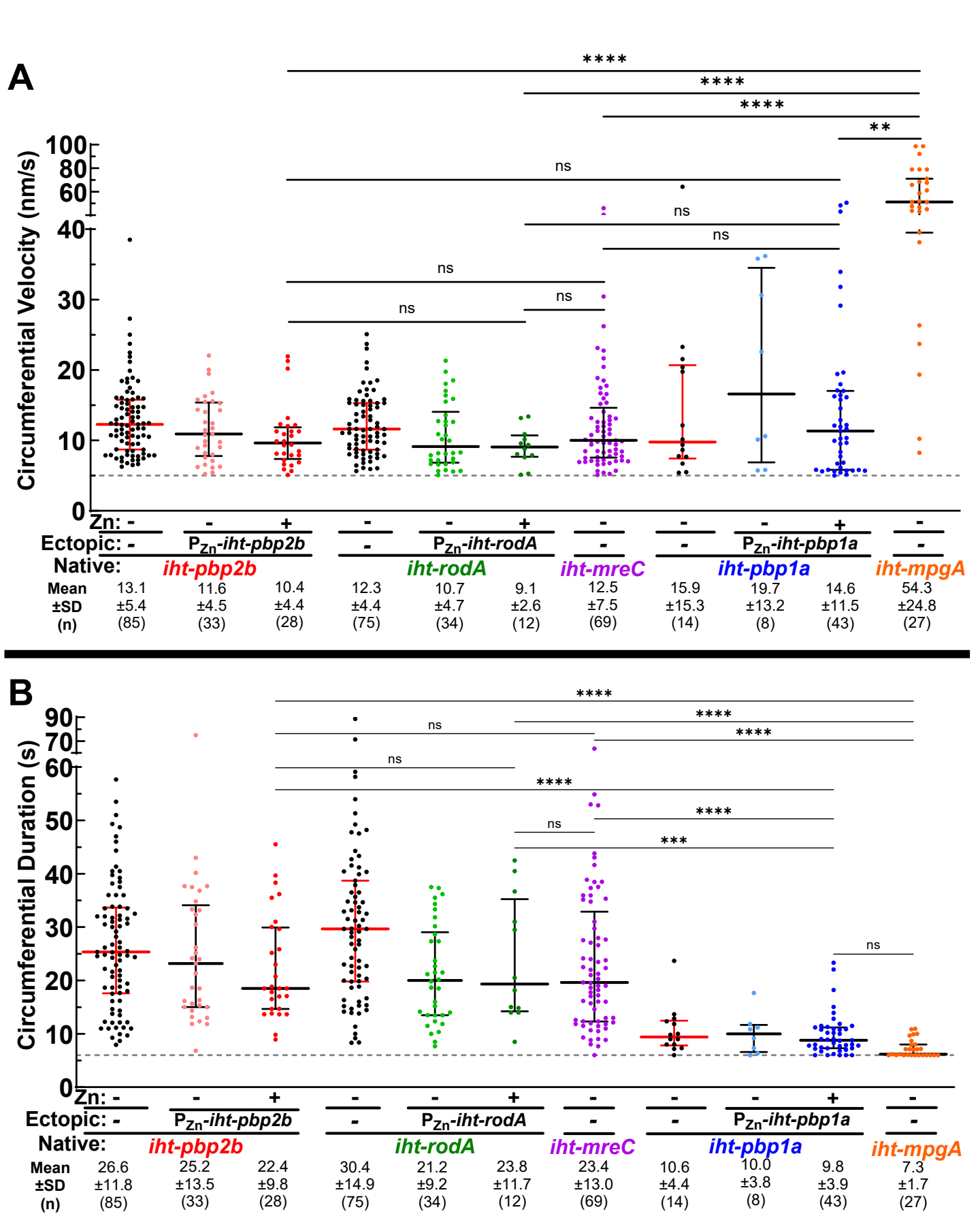
A
Circumferential Velocity (nm/s)
100
80
60
40
30
20
10
0
****
****
****
**
ns
ns
ns
ns
ns
ns
Zn: - - + - - + - - - + -
Ectopic: - PZn-iht-pbp2b - PZn-iht-rodA - - PZn-iht-pbp1a -
Native: iht-pbp2b iht-rodA iht-mreC iht-pbp1a iht-mpgA
Mean 13.1 11.6 10.4 12.3 10.7 9.1 12.5 15.9 19.7 14.6 54.3
±SD ±5.4 ±4.5 ±4.4 ±4.4 ±4.7 ±2.6 ±7.5 ±15.3 ±13.2 ±11.5 ±24.8
(n) (85) (33) (28) (75) (34) (12) (69) (14) (8) (43) (27)
B
Circumferential Duration (s)
90
70
60
50
40
30
20
10
0
****
****
****
ns
ns
****
****
ns
***
ns
Zn: - - + - - + - - - + -
Ectopic: - PZn-iht-pbp2b - PZn-iht-rodA - - PZn-iht-pbp1a -
Native: iht-pbp2b iht-rodA iht-mreC iht-pbp1a iht-mpgA
Mean 26.6 25.2 22.4 30.4 21.2 23.8 23.4 10.6 10.0 9.8 7.3
±SD ±11.8 ±13.5 ±9.8 ±14.9 ±9.2 ±11.7 ±13.0 ±4.4 ±3.8 ±3.9 ±1.7
(n) (85) (33) (28) (75) (34) (12) (69) (14) (8) (43) (27)

Fig. 3.

Fig. 3. bPBP2b, RodA, and MreC form a stable complex during active PG synthesis. Dot plots of (*A*) circumferential velocities and (*B*) circumferential durations of elongation PG synthesis proteins determined by sm-TIRFm at 1 FPS. Strains are the same as in Fig. 1. +Zn condition indicates 0.25 mM Zn inducer was added. Black and red lines are median ± interquartile, and mean ± SD are indicated. n = total molecules analyzed from 2-5 biological replicates. Dotted grey lines indicate the minimum thresholds for (*A*) velocity (5 nm/s) and (*B*) duration (6 s). A Kruskal-Wallis with Dunn's multiple comparisons test was used to compare circumferential velocities or circumferential durations in different strains. *ns* (nonsignificant); $^{**}P < 0.01$; $^{***}P < 0.001$; $^{****}P < 0.0001$.

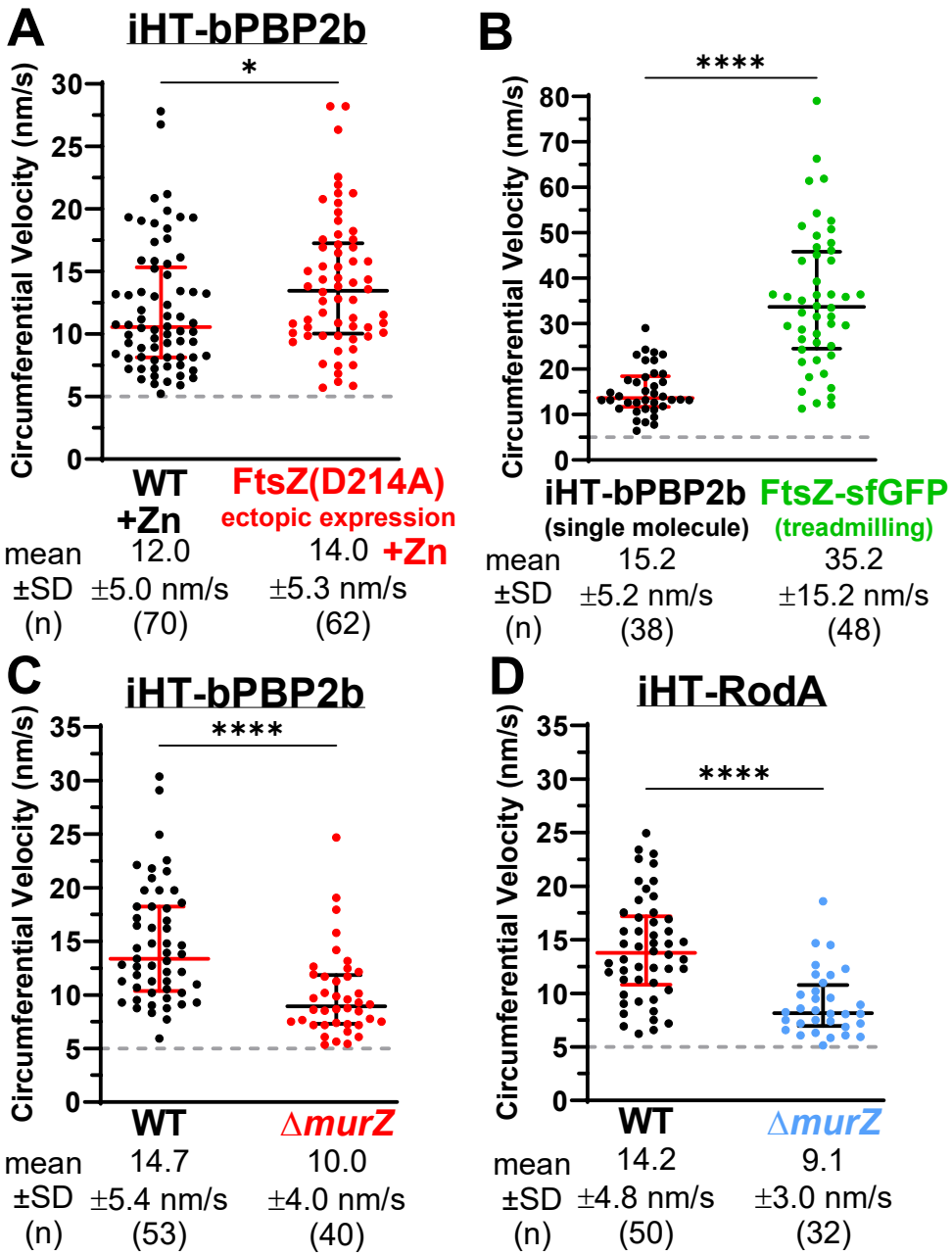

Fig. 4. Circumferential movement of bPBP2b and RodA is independent of FtsZ treadmilling and reflective of PG synthesis. Sm-TIRFm was performed at 1 FPS on strains expressing iHT-bPBP2b or iHT-RodA. Dot plots of circumferential velocities are shown. Black and red lines are median ± interquartile, and mean ± SD are indicated. (*A*) Both *iht-pbp2b* (black, IU15928) and *iht-pbp2b* P_{Zn}-*ftsZ*(D214A) (red, IU16091) strains were supplemented with 0.25 mM Zn inducer. (*B*) IU16056 expresses both iHT-bPBP2b and FtsZ-sfGFP. The treadmilling velocity of FtsZ-sfGFP filaments (green) and the circumferential velocity of iHT-bPBP2b single molecules (red) were determined. (*C*) *iht-pbp2b* (black, IU15928) and *iht-pbp2b* Δ*murZ* (red, IU16110) strains. (*D*) *iht-rodA* (black, IU15970) and *iht-rodA* Δ*murZ* (blue, IU16112) strains. n = total molecules analyzed from 2 biological replicates. Circumferential velocities in different strains were compared using a Mann-Whitney test. *$P < 0.05$; ****$P < 0.0001$.

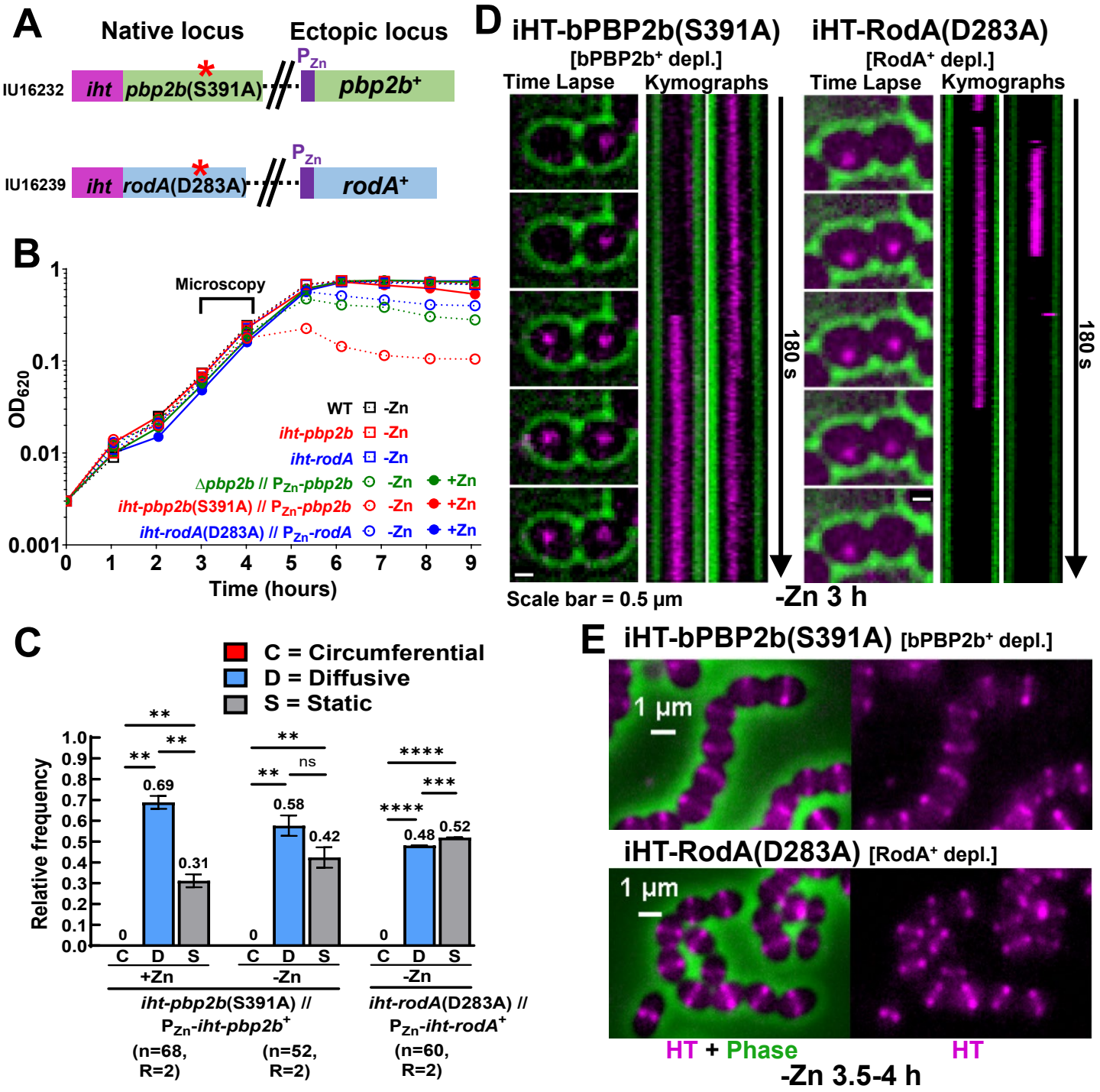
A
Native locus
Ectopic locus
IU16232
iht
pbp2b(S391A)
PZn
pbp2b+
IU16239
iht
rodA(D283A)
PZn
rodA+
B
Microscopy
OD620
Time (hours)
WT -Zn
iht-pbp2b -Zn
iht-rodA -Zn
Δpbp2b // PZn-pbp2b -Zn +Zn
iht-pbp2b(S391A) // PZn-pbp2b -Zn +Zn
iht-rodA(D283A) // PZn-rodA -Zn +Zn
C
C = Circumferential
D = Diffusive
S = Static
Relative frequency
0.69
0.31
0.58
0.42
0.48
0.52
+Zn
-Zn
-Zn
iht-pbp2b(S391A) //
PZn-iht-pbp2b+
(n=68,
R=2)
(n=52,
R=2)
iht-rodA(D283A) //
PZn-iht-rodA+
(n=60,
R=2)
D
iHT-bPBP2b(S391A)
[bPBP2b+ depl.]
iHT-RodA(D283A)
[RodA+ depl.]
Time Lapse
Kymographs
Time Lapse
Kymographs
180 s
180 s
Scale bar = 0.5 µm
-Zn 3 h
E
iHT-bPBP2b(S391A) [bPBP2b+ depl.]
1 µm
iHT-RodA(D283A) [RodA+ depl.]
1 µm
HT + Phase
HT
-Zn 3.5-4 h

Fig. 5.

Fig. 5. The catalytic activities of bPBP2b and RodA are required for cell viability and PG synthesis, but not localization. (*A*) Diagram of merodiploid strains containing catalytic mutant alleles fused to the HaloTag at the native locus and the Zn-inducible WT allele at the ectopic site. (*B*) Representative growth curves of WT (black square, IU1824), *iht-pbp2b* (red square, IU15928), *iht-rodA* (blue square, IU15970), Δ*pbp2b* // P_{Zn}-*pbp2b* (green, IU11258), *iht-pbp2b*(S391A) // P_{Zn}-*pbp2b* (red, IU16232), and *iht-rodA*(D283A) // P_{Zn}-*rodA* (blue, IU16239) strains grown in C+Y medium with or without 0.2 mM Zn inducer as described in the section on ectopic expression and depletion conditions in *Materials and Methods*. The experiment was repeated twice with similar results. (*C* and *D*) sm-TIRFm was performed at 1 FPS on strains IU16232 and IU16239. (*C*) Movement patterns of iHT-bPBP2b(S391A) (IU16232) and iHT-RodA(D283A) (IU16239). The layout is the same as Fig. 1*B* (see legend for details). Unpaired t-tests were performed to compare relative frequencies of motion types. *ns* (nonsignificant); $^{**}P < 0.01$; $^{***}P < 0.001$; $^{****}P < 0.0001$. (*D*) Representative montages and kymographs of static molecules from strains IU16232 and IU16239 (without Zn inducer for 3 h) are displayed as described for Fig. 1*A*, except the scale bar is 0.5 μm. (*E*) 2D-FM of catalytically inactive proteins. Strains IU16232 and IU16239 were grown without Zn (see Fig. 5*B*) and labeled with saturating amounts of HT-ligand. HT-fusion proteins are shown in magenta. Scale bar is 1 μm. The experiment was repeated twice with similar results.

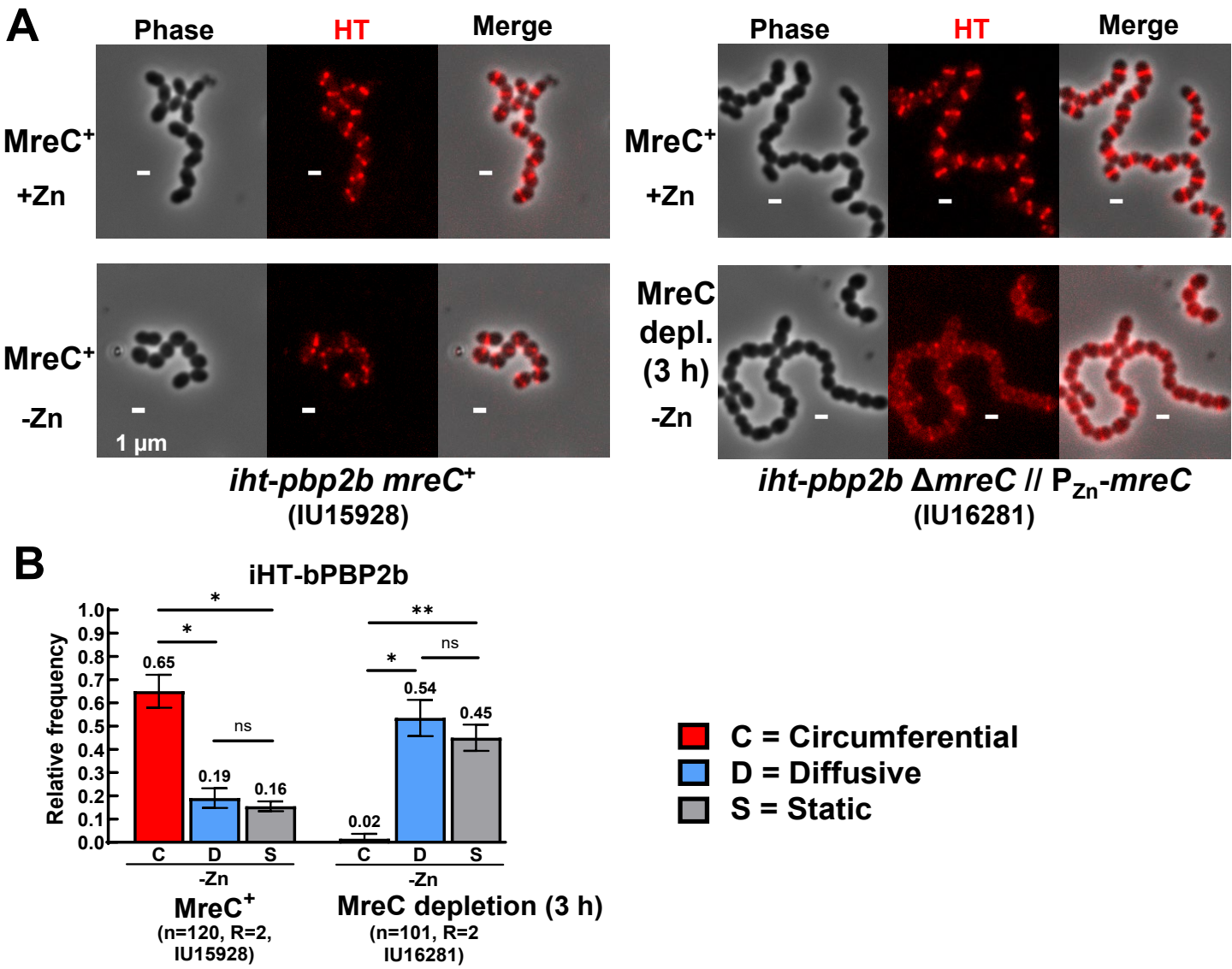

Fig. 6. bPBP2b localization becomes diffuse and circumferential movement is lost upon MreC depletion. (*A*) 2D-FM of strains *iht-pbp2b* (left, IU15928) and *iht-pbp2b* Δ*mreC* // P_{Zn}-*mreC* (right, IU16281). Cells were grown in C+Y media with or without (depletion) 0.2 mM Zn inducer, labeled with saturating amounts of HT-ligand, and imaged after 3 h. See the section on ectopic expression and depletion conditions in *Materials and Methods* for details. The experiment was repeated twice with similar results. (*B*) sm-TIRFm was performed at 1 FPS on strains *iht-pbp2b* (IU15928) and *iht-pbp2b* Δ*mreC* // P_{Zn}-*mreC* (IU16281) after 3 h of growth in C+Y media without Zn inducer (depletion). The layout is the same as Fig. 1*B* (see legend for details). Unpaired t-tests were performed to compare relative frequencies of motion types. *ns* (nonsignificant); $^{*}P < 0.05$; $^{**}P < 0.01$.

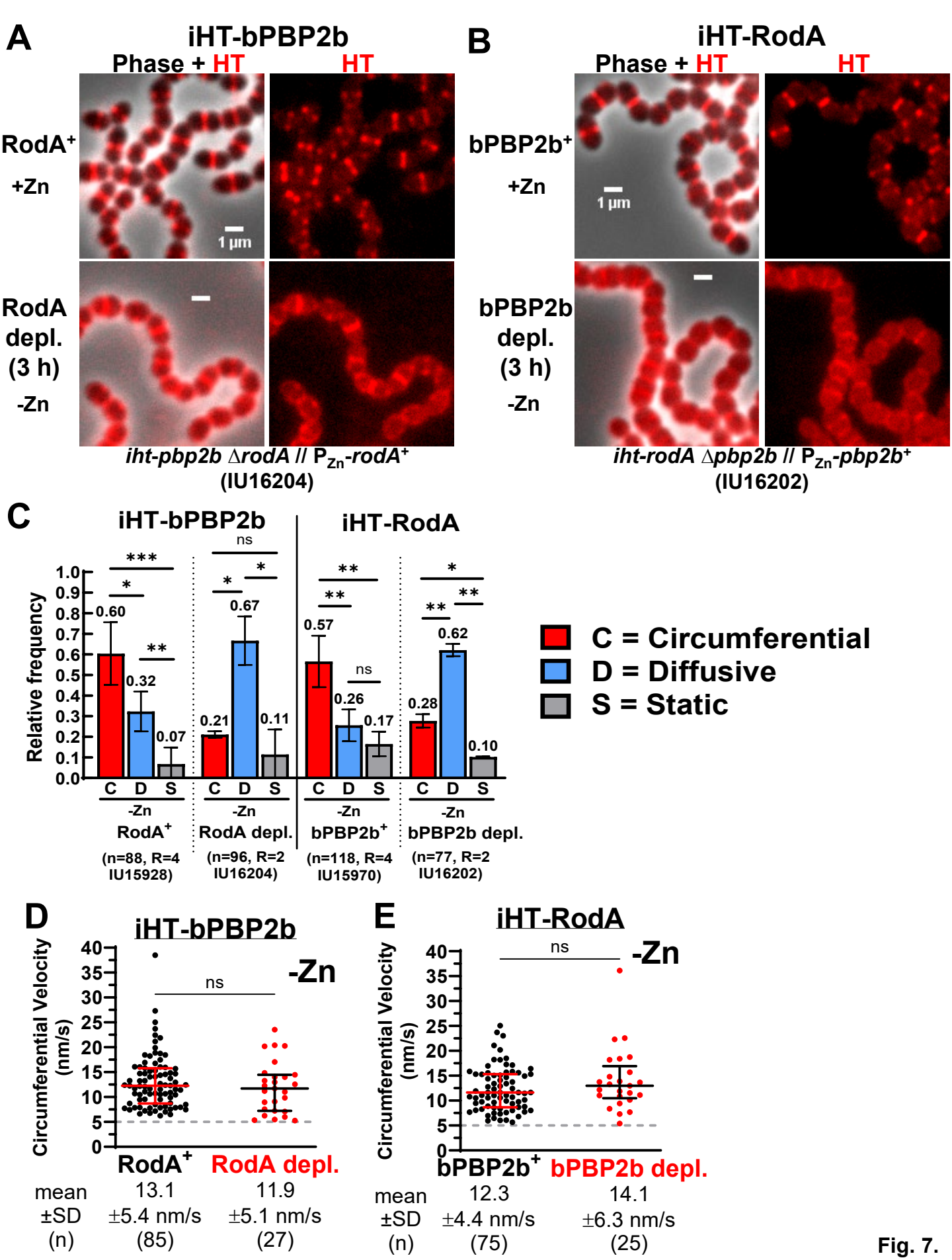
A
iHT-bPBP2b
Phase + HT
HT
RodA+
+Zn
1 µm
RodA
depl.
(3 h)
-Zn
iht-pbp2b ΔrodA // PZn-rodA+
(IU16204)
B
iHT-RodA
Phase + HT
HT
bPBP2b+
+Zn
1 µm
bPBP2b
depl.
(3 h)
-Zn
iht-rodA Δpbp2b // PZn-pbp2b+
(IU16202)
C
iHT-bPBP2b
iHT-RodA
Relative frequency
C = Circumferential
D = Diffusive
S = Static
-Zn
RodA+
(n=88, R=4
IU15928)
RodA depl.
(n=96, R=2
IU16204)
bPBP2b+
(n=118, R=4
IU15970)
bPBP2b depl.
(n=77, R=2
IU16202)
D
iHT-bPBP2b
-Zn
Circumferential Velocity (nm/s)
ns
RodA+
RodA depl.
mean ±SD (n)
13.1 ±5.4 nm/s (85)
11.9 ±5.1 nm/s (27)
E
iHT-RodA
-Zn
Circumferential Velocity (nm/s)
ns
bPBP2b+
bPBP2b depl.
mean ±SD (n)
12.3 ±4.4 nm/s (75)
14.1 ±6.3 nm/s (25)

Fig. 7.

Fig. 7. bPBP2b and RodA require each other for localization and motion. 2D-FM and sm-TIRFm at 1 FPS were performed on strains *iht-pbp2b* Δ*rodA* // P_{Zn}-*rodA* (IU16204) and *iht-rodA* Δ*pbp2b* // P_{Zn}-*pbp2b* (IU16202). (*A* and *B*) 2D-FM showing localization in cells of strains (*A*) iHT-bPBP2b (IU16204) and (*B*) iHT-RodA (IU16202) grown with or without (depletion; depl.) 0.2 mM Zn inducer for 3 h and labeled with saturating amounts of HT-ligand. See the section on ectopic expression and depletion conditions in *Materials and Methods* for additional details. The experiment was repeated twice with similar results. (*C* to *E*) sm-TIRFm was performed at 1 FPS on IU16204 and IU16202 without Zn inducer (depletion) for 3 hours. (*C*) Movement patterns of HT-labeled molecules. Results for the *iht-pbp2b* Δ*rodA* // P_{Zn}-*rodA* (IU16204) and *iht-rodA* Δ*pbp2b* // P_{Zn}-*pbp2b* (IU16202) strains were determined and are graphed with data for *iht-pbp2b* (IU15928) and *iht-rodA* (IU15970) replotted from Fig. 1*B* for comparison. The layout is the same as Fig. 1*B* (see legend for details). Unpaired t-tests were performed to compare relative frequencies of motion types. *ns* (nonsignificant), $^{*}P < 0.05$; $^{**}P < 0.01$; $^{***}P < 0.001$. (*D* and *E*) Dot plots of circumferential velocities with mean values ± SD indicated for (*D*) strains IU15928 (black) and IU16204 (red), and (*E*) strains IU15970 (black) and IU16202 (red). Data from stains IU15928 and IU15970 are replotted from Fig. 3*A* for comparison. Black and red lines are median ± interquartile, and mean ± SD are indicated. n = total molecules analyzed from 2 biological replicates. A Mann-Whitney test was used to compare velocities upon protein depletion (depl.). *ns* (nonsignificant).

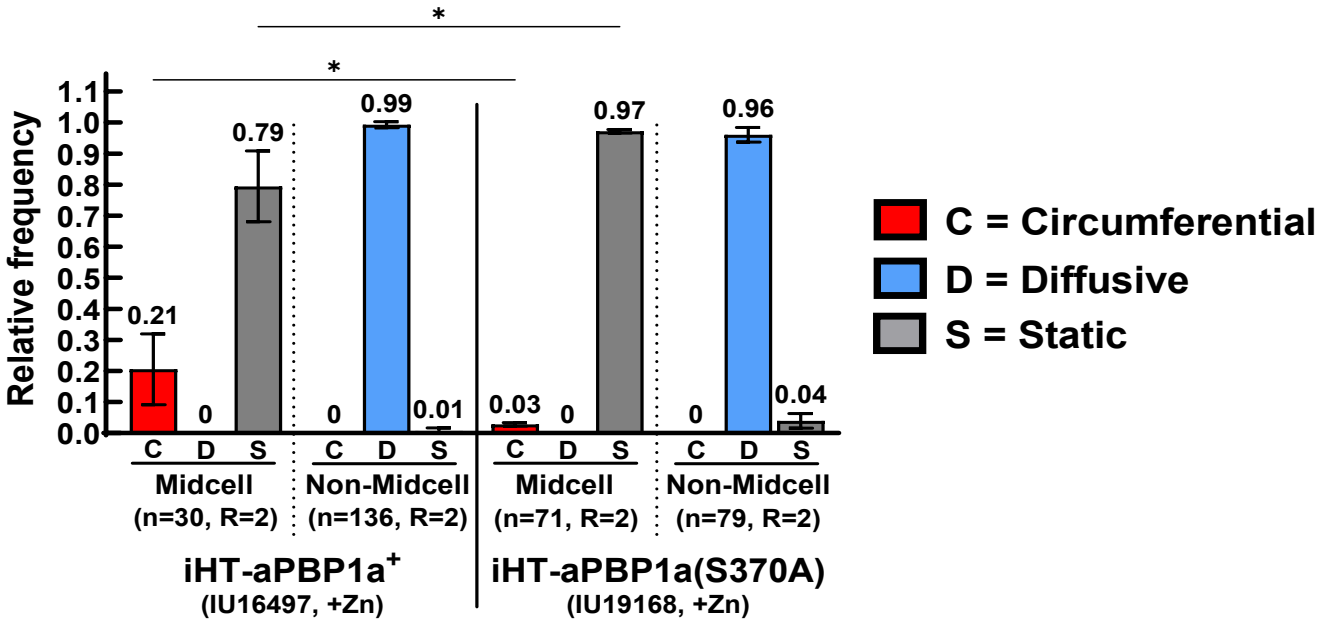

Fig. 8. Circumferential movement of aPBP1a reflects active PG synthesis. Sm-TIRFm was performed at 1 FPS as described in *Materials and Methods* on strains *iht-pbp1a* // P_{Zn}-*iht-pbp1a* (IU16497) and *iht-pbp1a*(S370A) // P_{Zn}-*iht-pbp1a*(S370A) (IU19168) with 0.25 mM Zn added. Movement patterns of HT-labeled molecules at sites of PG synthesis (midcell) or elsewhere in the cell (non-midcell) were analyzed. The layout is the same as Fig. 1*B* (see legend for details). A two-way ANOVA with Tukey's multiple comparison test was used to compare relative frequencies of motion types among strains. *$P < 0.05$.

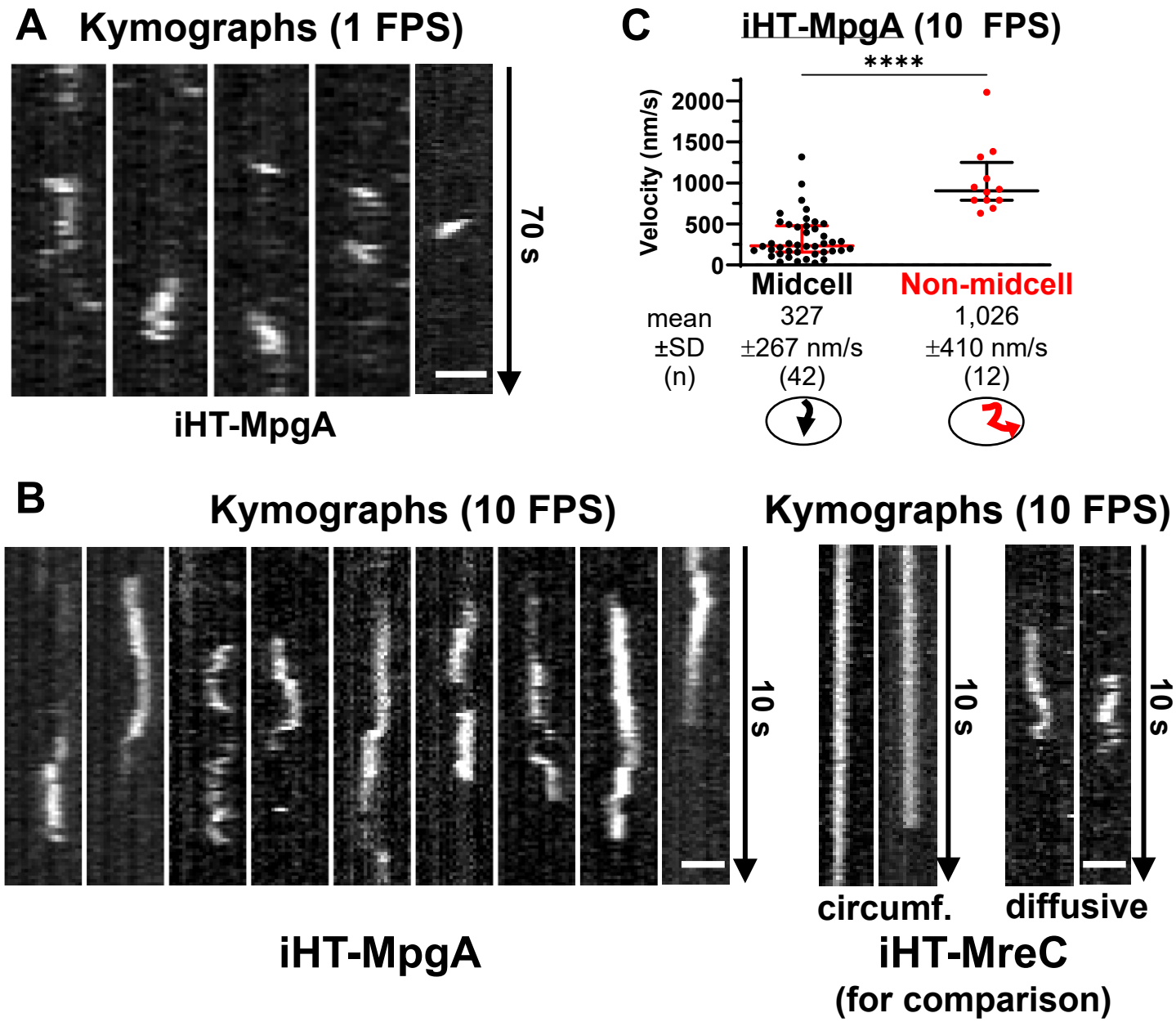

Fig. 9. MpgA displays confined subdiffusive movement at midcell. Sm-TIRFm was performed on strains *iht-mpgA* (IU15997) and *iht-mreC* (IU16344). Representative kymographs of (*A*) iHT-MpgA molecules moving at sites of PG synthesis imaged at 1 FPS and (*B*) iHT-MpgA and iHT-MreC molecules imaged at 10 FPS. (*C*) Dot plots of velocities determined at 10 FPS over short runs of iHT-MpgA molecules in midcell regions (black) and at non-midcell regions (red). Black and red lines are median ± interquartile, and mean ± SD are indicated. n = total molecules analyzed from 2 biological replicates. Velocities in different regions of cells were compared using a Mann-Whitney test. ****$P < 0.0001$.

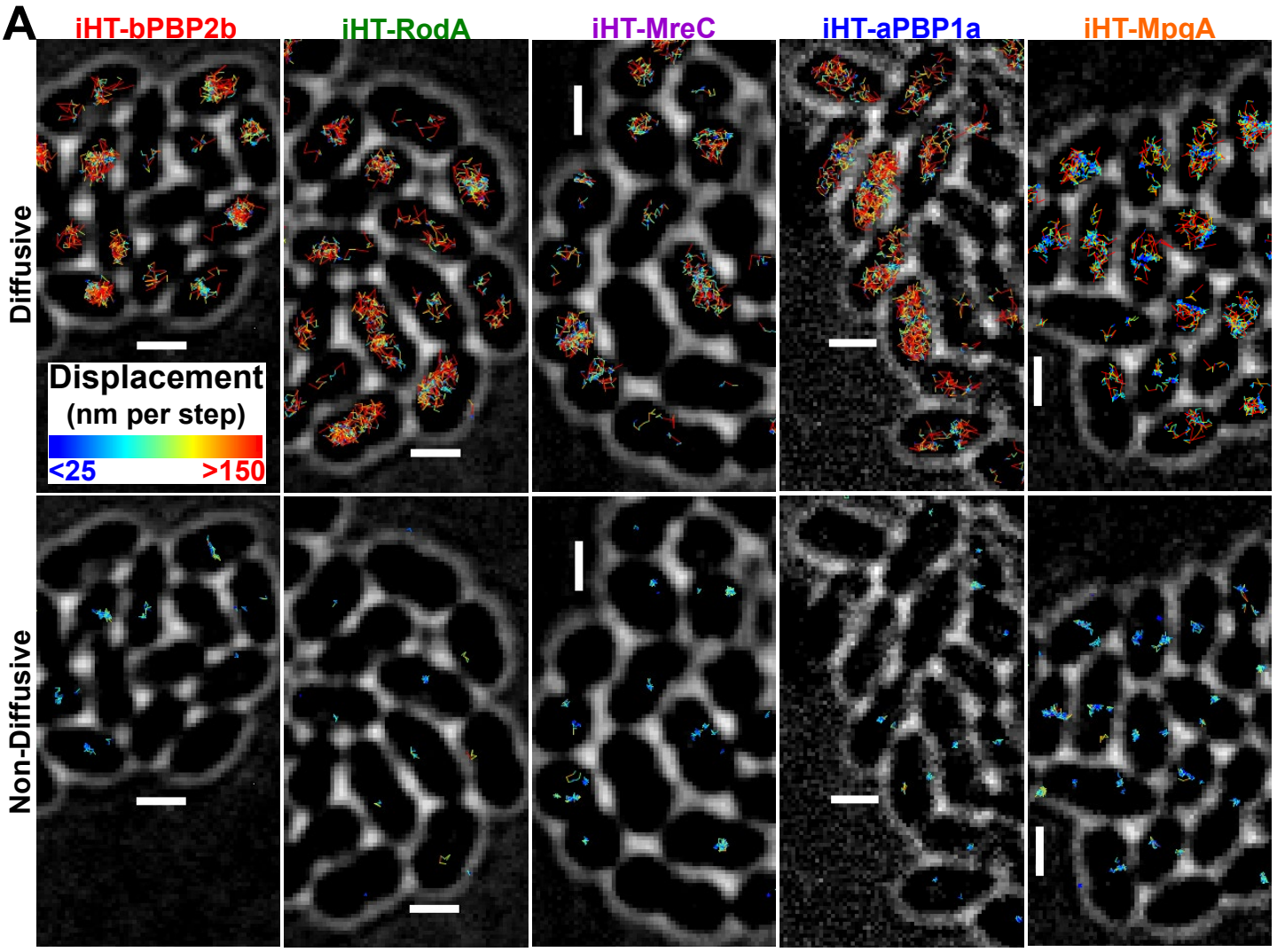

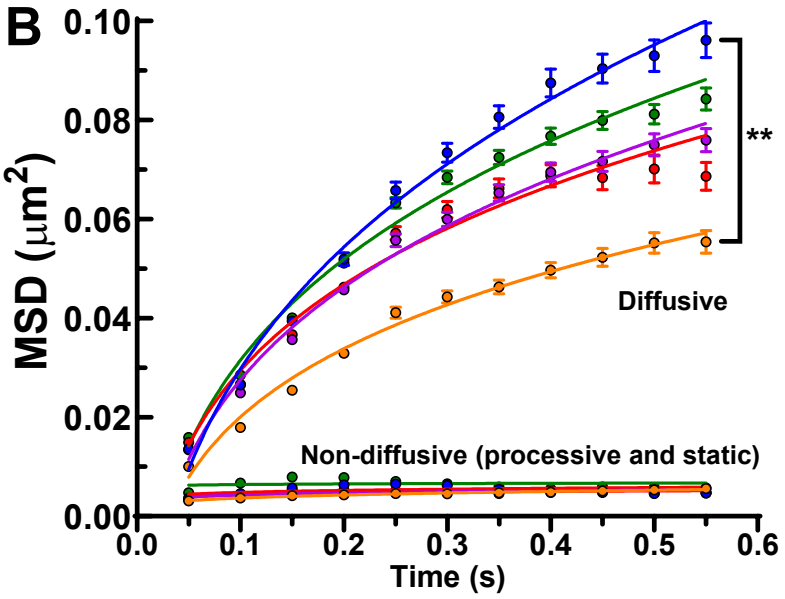

	Diffusion coefficient ($\mu m^2/s$) ±SEM	α	% diffusive	n
iht-pbp1a // P_{Zn}-*iht-pbp1a* +Zn	0.055 ±0.0005	0.28	77	914
iht-rodA // P_{Zn}-*iht-rodA* +Zn	0.050 ±0.0002	0.23	90	2,116
iht-mreC	0.047 ±0.0003	0.22	68	1,351
iht-pbp2b // P_{Zn}-*iht-pbp2b* +Zn	0.046 ±0.0003	0.20	74	1,143
iht-mpgA	0.040 ±0.0003	0.18	60	1,291

Fig. 10.

Fig. 10. Components of the pneumococcal core PG elongasome and proteins implicated in elongation PG synthesis exhibit different patterns of confined diffusion. Sm-TIRFm was performed at 20 FPS on strains *iht-pbp2b* // P_{Zn}-*iht-pbp2b* (IU16553), *iht-rodA* // P_{Zn}-*iht-rodA* (IU16496), *iht-mreC* (IU16344), *iht-pbp1a* // P_{Zn}-*iht-pbp1a* (IU16497) and *iht-mpgA* (IU15997). 0.25 mM Zn inducer was added to strains IU16553, IU16496 and IU16497. (*A*) Representative fields of cells containing multiple single-molecule trajectories (colored lines) classified as diffusive (top row) and non-diffusive (bottom row). Trajectories with a displacement > 0.13 μm and a velocity standard deviation > 0.63 μm/s were defined as diffusive, and the remaining trajectories were defined as non-diffusive. Full details of trajectory constructions and classification criteria are described in *Materials and Methods*. The color of each trajectory line segment represents the displacement (in nm) of the molecule from one frame to the next. Scale bar is 1 μm. (*B*) Mean square displacements (MSD) were calculated for diffusive and non-diffusive trajectories. Circles show MSD values, and error bars represent SEM. Lines represent MSD curves fit to the data as described in *Materials and Methods*. To the right of the graph are the mean diffusion coefficients (± SEM) of diffusive trajectories, alpha values of diffusive trajectories (α), the percent of total trajectories that were classified as diffusive (% diffusive), and the total number of trajectories (n) analyzed from 2 biological replicates. α values < 1 indicate that molecules are exhibiting confined diffusion (or subdiffusion), discussed in the text. The diffusion coefficients were compared between strains using a Brown-Forsythe and Welch's ANOVA with a Games-Howell multiple comparisons test. $^{**}P < 0.01$.

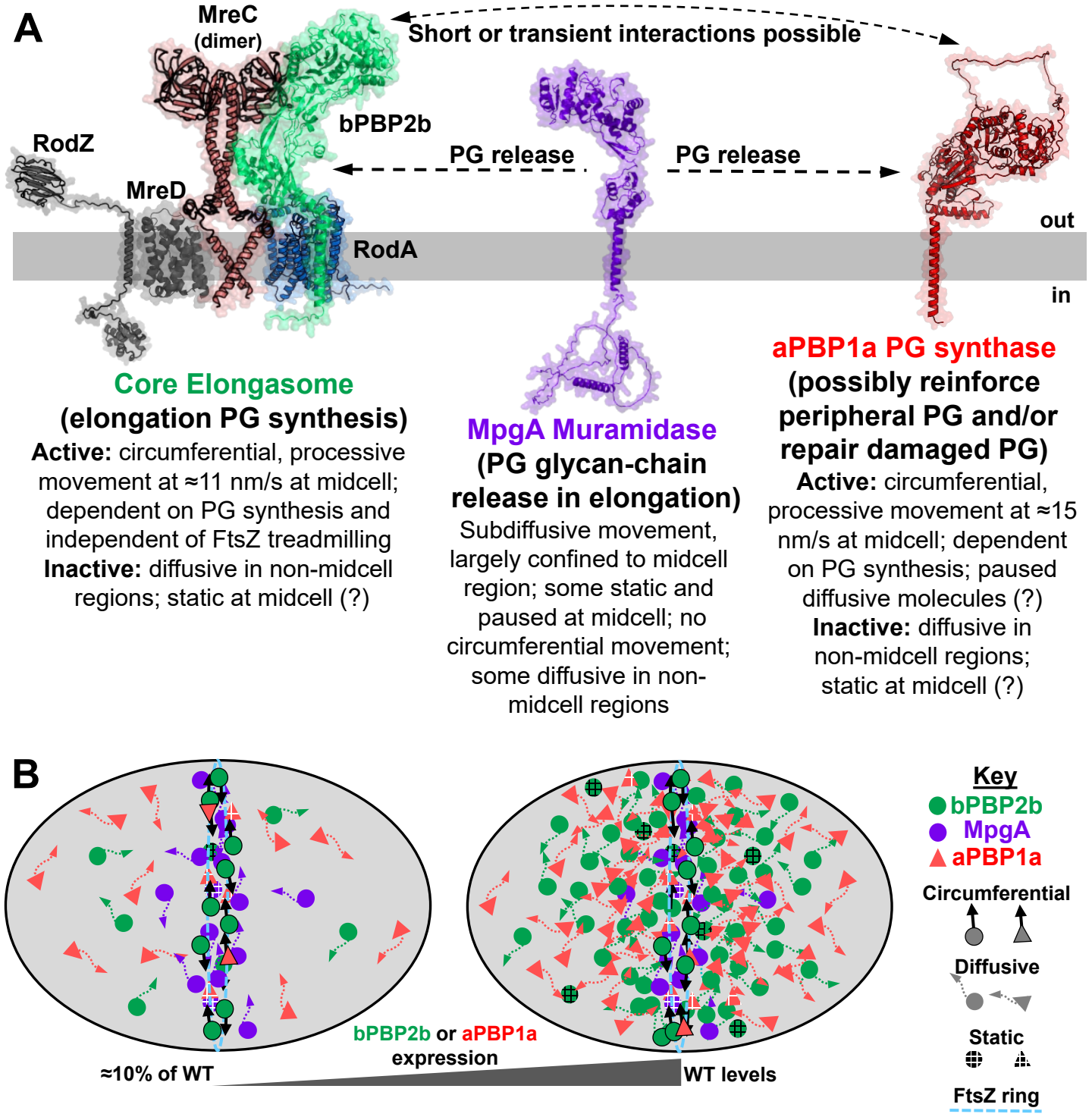
A
MreC
(dimer)
Short or transient interactions possible
bPBP2b
RodZ
PG release
PG release
MreD
out
RodA
in
Core Elongasome
(elongation PG synthesis)
Active: circumferential, processive movement at ≈11 nm/s at midcell; dependent on PG synthesis and independent of FtsZ treadmilling
Inactive: diffusive in non-midcell regions; static at midcell (?)
MpgA Muramidase
(PG glycan-chain release in elongation)
Subdiffusive movement, largely confined to midcell region; some static and paused at midcell; no circumferential movement; some diffusive in non-midcell regions
aPBP1a PG synthase
(possibly reinforce peripheral PG and/or repair damaged PG)
Active: circumferential, processive movement at ≈15 nm/s at midcell; dependent on PG synthesis; paused diffusive molecules (?)
Inactive: diffusive in non-midcell regions; static at midcell (?)
B
bPBP2b or aPBP1a
expression
≈10% of WT
WT levels
Key
bPBP2b
MpgA
aPBP1a
Circumferential
Diffusive
Static
FtsZ ring

Fig. 11.

Fig. 11. Summary model of (*A*) the composition and dynamics of core elongasome components (bPBP2b, RodA, and MreC) and proteins linked to PG elongation synthesis (aPBP1a and MpgA) in growing *S. pneumoniae* cells; and (*B*) the distribution of these proteins when underexpressed (left) or expressed at WT levels (right). (*A*) The circumferential, processive movement of bPBP2b, RodA, and MreC reported here likely apply to the other core elongasome components RodZ and MreD. In early, predivisional cells, the core PG elongasome is located in the FtsZ-ring at the equator midcell of a daughter cell. In later divisional cells, the core PG elongasome is in the outer ring of the midcell septal annular disk. The motion of MreC is the same in early or late divisional cells. Class A aPBP1a also displays circumferential, processive motion at midcell that depends on PG synthesis, but its dynamics indicate that aPBP1a is not a persistent member of the core PG elongasome, although short interactions are possible. In contrast, MpgA moves in a distinctive type of subdiffusion that is largely confined to the midcell region. Components of the core elongasome and aPBP1a move diffusively outside of midcell rings. There are also nonmoving, static molecules (> 6 s) of elongasome proteins and aPBP1a, mainly in midcell regions. It is not clear whether static molecules are synthesizing PG or are in a non-synthesizing transition state. In addition, diffusing molecules of aPBP1a and MpgA were infrequently detected pausing (< 1s) before resuming motion. See text for additional information. (*B*) When underexpressed, components of the core PG elongasome are largely confined to PG synthesis at midcell septa and the equators of predivisional daughter cells starting to divide. In contrast, when expressed at WT levels, most components of the PG elongasome (and aPBP1a) are diffusing over the cell surface and are not synthesizing PG. Thus, elongasome components and aPBP1a are in excess in growing cells, and only a limited number engage in midcell PG synthesis. In contrast, subdiffusion of MpgA molecules expressed at the WT level is largely confined to the midcell region by an unknown mechanism. See text for additional details.